Protein absorption in the zebrafish gut is regulated by interactions between lysosome rich enterocytes and the microbiome

Laura Childers,[1] Jieun Park,[2,3] Siyao Wang,[1] Richard Liu,[1] Robert Barry,[4] Stephen A. Watts,[4] John F. Rawls,*[5] and Michel Bagnat*[1,6]

[1]Department of Cell Biology, Duke University, Durham, NC 27710, USA
[2]Neuroscience Center, University of North Carolina, Chapel Hill, NC 27599, USA
[3]Carolina Institute of Developmental Disabilities, Chapel Hill, NC 27510, USA
[4]Department of Biology, University of Alabama at Birmingham, Birmingham, Al, 35294, USA
[5]Department of Molecular Genetics and Genomics, Duke University, Durham, NC 27710, USA
[6]Lead Contact

*Correspondence:
michel.bagnat@duke.edu
john.rawls@duke.edu

Abstract

Dietary protein absorption in neonatal mammals and fishes relies on the function of a specialized and conserved population of highly absorptive lysosome rich enterocytes (LREs). The gut microbiome has been shown to enhance absorption of nutrients, such as lipids, by intestinal epithelial cells. However, whether protein absorption is also affected by the gut microbiome is poorly understood. Here, we investigate connections between protein absorption and microbes in the zebrafish gut. Using live microscopy-based quantitative assays, we find that microbes slow the pace of protein uptake and degradation in LREs. While microbes do not affect the number of absorbing LRE cells, microbes lower the expression of endocytic and protein digestion machinery in LREs. Using transgene assisted cell isolation and single cell RNA-sequencing, we characterize all intestinal cells that take up dietary protein. We find that microbes affect expression of bacteria-sensing and metabolic pathways in LREs, and that some secretory cell types also take up protein and share components of protein uptake and digestion machinery with LREs. Using custom-formulated diets, we investigated the influence of diet and LRE activity on the gut microbiome. Impaired protein uptake activity in LREs, along with a protein-deficient diet, alters the microbial community and leads to increased abundance of bacterial genera that have the capacity to reduce protein uptake in LREs. Together, these results reveal that diet-dependent reciprocal interactions between LREs and the gut microbiome regulate protein absorption.

Introduction

The ability of the intestine to efficiently absorb nutrients from the diet is influenced significantly by the microbiome that it harbors (A. S. Wilson et al. 2020; Kau et al. 2011). Most dietary nutrients, including proteins, lipids, and carbohydrates, are absorbed by the small intestinal epithelium after luminal digestion. In zebrafish and mice, microbiome colonization enhances small intestinal absorption of dietary lipids compared to germ-free (GF) animals (Semova et al. 2012; Martinez-Guryn et al. 2018). Gut microbiomes are also known to increase

dietary energy harvest by fermenting complex carbohydrates into short-chain fatty acids that can be absorbed by the gut epithelium (Cholan et al. 2020). There is evidence that *Drosophila*-associated microbes absorb dietary proteins and amino acids and are, in turn, ingested and metabolized by the host, promoting survival under dietary protein-limited conditions (Keebaugh et al. 2018; Yamada et al. 2015; Lesperance and Broderick 2020). Furthermore, amino acids secreted by the *Drosophila* microbiome have been shown to modify feeding behavior (Kim et al. 2021). However, whether the microbiome affects intestinal absorption of dietary proteins remains poorly understood. The importance of this question is underscored by the gut microbiome's links to protein malnutrition diseases. Children with kwashiorkor, a disease caused by severe protein malnutrition, have significantly altered gut microbiomes that promote weight loss when transplanted into GF mice (Smith et al. 2013). These studies suggest that protein deprivation may cause a gut microbial community to develop that further exacerbates the effects of the disease. Defining the reciprocal interactions between intestinal physiology, microbiome, and dietary protein nutrition is therefore an important research goal.

In neonatal mammals and fishes, dietary protein absorption is dependent on the function of a specialized population of epithelial cells in the ileal region of the small intestine originally described as vacuolated or neonatal enterocytes (Kraehenbuhl and Campiche 1969; Rodríguez-Fraticelli et al. 2015; Wallace et al. 2005; Gonnella and Neutra 1984; J. M. Wilson, Whitney, and Neutra 1987; Rombout et al. 1985; Graney 1968). Recent work in zebrafish and mice showed that these cells, which we refer to as lysosome rich enterocytes (LREs), are highly endocytic and specialize in the uptake of luminal proteins that they then digest in giant lysosomal vacuoles (Park et al. 2019). In mammals, LREs are present only during suckling stages and are lost at weaning (Harper et al. 2011), whereas in fishes they are retained through adult life (Park et al. 2019; Noaillac-Depeyre and Gas 1976; Stroband and Debets 1978). In zebrafish, digestive processes can be observed live in the transparent larvae following gavage with fluorescent cargoes directly into the intestinal lumen (Park et al. 2019; Rodríguez-Fraticelli et al. 2015). Using this assay, LREs were shown to internalize proteins but not lipids from the intestinal lumen (Park et al. 2019).

LREs internalize luminal proteins using an endocytic complex composed of the scavenger receptor cubilin (Cubn), the transmembrane linker amnionless (Amn), and endocytic clathrin adaptor Dab2 (Park et al. 2019). Loss of these components severely reduces their capacity to take up luminal proteins, leading to stunted growth, poor survival, and intestinal edema reminiscent of kwashiorkor (Park et al. 2019). LREs are broadly present in vertebrates and likely also in lower chordates (Nakayama, Sekiguchi, and Ogasawara 2019; Yonge 1923), suggesting LRE development and physiology are ancient and important aspects of intestinal function. However, whether gut microbes play a role in LRE dependent processes or the pathobiology of LRE deficiency is not known.

Previous work suggested that microbes affect uptake and degradation kinetics in LREs. Specifically, zebrafish larvae colonized with a complex gut microbiome (ex-GF conventionalized or CV) had electron-dense material in the lysosomes of LREs that was not detected in GF larvae (Rawls, Samuel, & Gordon, 2004). Consistent with these findings, CV larvae immersed in horse radish peroxidase (HRP) had increased HRP accumulation in LREs (Bates et al., 2006). However, it was unclear from those studies if microbes caused material to accumulate in LREs by increasing the rate of LRE uptake, decreasing LRE degradation, or both.

Here, we investigate how interactions between LREs, the gut microbiome, and diet affect host nutrition in zebrafish larvae. We demonstrate that the gut microbiome reduces the rates of protein uptake and degradation in LREs. We present single-cell RNA sequencing (scRNA-seq) data that represents all major intestinal cell types, uncovering cell populations capable of protein

uptake, and the effects of microbes across the gut. Using monoassociation experiments, we dissected the effects of specific microbial strains on LREs and found that *Vibrio cholerae* colonization strongly reduces LRE activity. Finally, using 16S rRNA gene sequencing and custom formulated diets, we found that dietary protein content and LRE activity also affect the gut microbiome composition. Together, our results uncover significant interactions between LREs, diet, and gut microbes that regulates host nutrition.

RESULTS

Gut microbiome slows uptake and degradation kinetics in LREs

We first investigated if microbes affect protein absorption in LREs. To do this, we used established methods (Pham et al. 2008) to rear zebrafish to the larval stage in gnotobiotic conditions to compare LRE activity in GF and ex-GF conventionalized (CV) conditions. In these experiments, a portion of the GF cohort was conventionalized with microbes at 3 days post fertilization (dpf), while the rest remained in the GF condition until the experimental endpoint of 6 dpf. At that point, we gavaged GF and CV larvae with fluorescent soluble cargoes and imaged uptake in the LRE region using confocal microscopy (Figure 1A) (Park et al. 2019; Shaner et al. 2004; Cocchiaro and Rawls 2013). To test how the microbiome affects protein uptake in LREs, we gavaged larvae with the purified fluorescent protein mCherry (Shaner et al. 2004). Previous work showed that LREs readily take up mCherry following gavage with fluorescence peaking in the anterior LREs (Park et al. 2019). We found that GF and CV larvae rapidly took up mCherry in the LREs, absorbing detectable levels of mCherry within five minutes of gavage (Figure 1B-1C). LREs progressively became more saturated with mCherry between 5 – 60 minutes post gavage in both conditions (Figure 1B-1C). However, mCherry fluorescence peaked in the anterior LREs of GF larvae by 40 minutes PG (Figure S1A), but the peak did not emerge until 60 minutes PG in CV larvae (Figure S1B). Between 5 and 60 minutes PG, the anterior LREs of GF larvae accumulated mCherry at a significantly faster rate than those in CV larvae (Figure S1C). Across the entire LRE region, GF larvae took up significantly more mCherry than CV larvae by 1 hour PG (Figure 1D). However, LREs in CV larvae eventually reached a similar level of mCherry uptake by 5 hours PG (Figure 1E). Over the 1 to 5 hour time course, the anterior LREs in CV larvae gradually increased in mCherry saturation, while mCherry saturation remained at a stable, high level in GF larvae (Figure S1D). We tested if the gut microbiome reduces mCherry uptake in LREs by lowering its concentration in the lumen. That did not appear to be the case because luminal mCherry concentrations were equivalent in GF and CV larvae at 1 and 5 hours PG (Figure S1E), and the microbiome did not degrade mCherry over time (Figure S1F). We observed a similar trend using Lucifer Yellow (LY) as a fluid phase endocytic tracer (Swanson, Yirinec, and Silverstein 1985; Park et al. 2019). GF larvae took up significantly more LY than CV larvae by 1 hour PG (Figure 1F) but accumulated similar amounts by 3 hours PG (Figure S1G). These results suggest that microbial colonization reduces the rate of endocytosis in the LRE region.

We hypothesized that microbial burden may influence the rate of luminal uptake and that a threshold density may be needed for microbes to affect protein-uptake kinetics in LREs. To investigate this possibility, we compared mCherry uptake activity between CV larvae with different microbial densities. At 1 hour PG, mCherry uptake was not reduced in CV larvae when the density was 3×10^5 CFU/mL in the gnotobiotic zebrafish media (GZM) (Figure S1H). However, a higher density of 3×10^6 CFU/mL in the GZM was sufficient to significantly reduce mCherry uptake in CV larvae compared to GF larvae (Figure S1I).

141 LREs degrade much of the protein they take up from the intestinal lumen within their
142 lysosomal vacuole (Park et al. 2019). To test if microbes affect the protein degradation process,
143 we employed a pulse-chase assay (Park et al. 2019) to compare the rate of protein degradation
144 between GF and CV larvae (Figure 2A). At 6 dpf, larvae were gavaged with mTurquoise (25
145 mg/mL), a pH-insensitive protein that degrades rapidly in LREs (Figure S2). One hour after
146 gavage, the remaining luminal mTurquoise was flushed with PBS, and live larvae were imaged
147 with confocal microscopy over the course of 1 hour. In both GF and CV larvae, mTurquoise
148 degraded over the 1-hour imaging time course (Figure 2B – 2C), with the degradation process
149 occurring at a significantly faster rate in GF compared to CV LREs (Figure 2D). Together, these
150 uptake and degradation kinetics assays demonstrate that the microbiome reduces the rate of
151 cargo uptake and lysosomal protein degradation in LREs.
152
153 **Identification of two microbe-independent LRE cell clusters and a microbe-dependent**
154 **cloaca cluster**
155 Given the differences we observed in LRE kinetics between GF and CV larvae, we wanted
156 to investigate how the gut microbiome impacts gene expression programs in LREs and other
157 intestinal cells. To do so, we prepared GF or CV *TgBAC(cldn15la-GFP)* transgenic larvae (Alvers
158 et al. 2014), in which all intestinal cells are GFP-positive, and then gavaged them with mCherry
159 to label LREs and other cells at 6 dpf (Figure 3A). At 3 hours PG, we isolated mCherry-
160 positive/GFP-positive and mCherry-negative/GFP-positive cells by fluorescent-activated cell
161 sorting (FACS) as previously described (Park et al. 2019) and processed them for scRNA-seq.
162 Clustering analysis with Seurat (Satija et al. 2015) revealed seventeen cell clusters,
163 including two LRE clusters (Figure 3B). Each of these clusters was characterized by
164 transcriptomic signatures that distinguished them from other clusters (Figure 3C) (Supplementary
165 Tables A – C). Ileocytes are an ileal enterocyte population that specialize in bile salt recycling
166 (Wen et al. 2021). Interestingly, *fatty acid binding protein 6* (*fabp6*), a top ileocyte cluster marker,
167 was also expressed in both LRE clusters (Figure 3C). Using transgenic reporters, previous studies
168 showed that *fabp6* expression is highest in the ileocytes, but expression was also detected in the
169 anterior LRE region (Wen et al. 2021; Lickwar et al. 2017). We, therefore, termed the LRE cluster
170 with the higher *fabp6* expression in our scRNAseq dataset "anterior LREs" and the LRE cluster
171 with lower *fabp6* expression "posterior LREs". In total, this dataset includes 131 GF and 199 CV
172 anterior LREs, along with 359 GF and 381 CV posterior LREs (Figure S3A).
173 GF and CV larvae had proportionally similar numbers of cells in each cluster, including
174 LREs (Figure S3B), with the exception of a cluster we called Cloaca 3, which was only present in
175 the CV condition (Fig 3D). GO term analysis revealed that Cloaca 3 consisted of IECs that are
176 enriched in pathways related to host defense, response to bacteria, and iron ion transport (Fig
177 S3C). Several of the genes involved in bacterial response were top cluster markers for Cloaca 3
178 (Figure S3D). These include genes involved in sensing bacteria through lipopolysaccharide-
179 binding, neutrophil recruitment, and inflammation (Kanther et al. 2011). Their expression was
180 markedly higher in Cloaca 3 than neighboring clusters (Figure S3E). For example, one of the
181 Cloaca 3 marker genes was serum amyloid a (*saa*), which is known to be induced by microbiota
182 in the distal intestine and cloaca (Murdoch et al. 2019). These results suggest that development
183 of Cloaca 3 cells is stimulated by the microbiome and functions in microbial sensing and immune
184 response.
185 Our scRNAseq data indicated that LRE numbers were similar in the presence or absence
186 of the gut microbiome (Figure S3A). To quantitatively determine if microbes affect the number of
187 LREs, we gavaged DQ-red BSA to mark the LRE lysosomes (Marwaha and Sharma 2017) in GF

188 and CV larvae and computationally segmented LREs using ilastik (Sommer et al. 2011) (Figure
189 S3F). This experiment revealed that there is not a significant difference in the number of active
190 LREs between GF and CV larvae (Figure 3E). Together, these data show that the development
191 of most intestinal cell clusters, including LREs, is not dependent on the gut microbiome. The
192 notable exception is Cloaca 3, which only appeared in the presence of gut microbes.
193
194 **Identification of cell types with protein uptake capacity**
195 Next, we explored the effects of the gut microbiome on mCherry uptake throughout the
196 gut. Surprisingly, scRNA-seq analysis revealed that mCherry is internalized by several cell types
197 in addition to LREs (Figure 4A–B). While LREs had the highest percentage of mCherry-positive
198 cells, other mCherry-positive cell types included ileocytes, goblet, acinar, enteroendocrine,
199 immune and *best4/otop2* cells in both GF and CV conditions (Figure 4C). Notably, anterior
200 enterocytes, pharynx, and cloaca clusters contained extremely low levels of mCherry-positive
201 cells (Figure 4C), showing that these cell types have very low protein uptake activity.
202 The gut microbiome increased the proportions of mCherry-positive cells in several clusters
203 (Figure 4D). This effect could be observed in secretory cells such as enteroendocrine, goblet
204 cells, and acinar cells, which increased by 25%, 11%, and 8%, respectively. The gut microbiome
205 also increased the proportion of mCherry-positive neurons by 13%. Notably, the proportion of
206 mCherry-positive anterior (84 – 91%) and posterior (98 – 97%) LREs was extremely high in both
207 GF and CV conditions, respectively (Figure 4C). However, the gut microbiome had mixed effects
208 on the number of mCherry-positive LREs. While anterior LREs had a slightly higher proportion of
209 mCherry-positive cells in the CV condition (7% increase), microbes caused a small decrease in
210 the proportion of mCherry-positive posterior LREs (1% decrease) (Figure 4C–D). Regardless of
211 microbial colonization, the proportion of mCherry-positive LREs remained high, underscoring the
212 robust protein-uptake program in these cells.
213 Since the microbiome increased the proportion of mCherry-positive cells in many clusters,
214 we proceeded to investigate the transcriptional program they hold in common. There were many
215 differentially expressed genes between aggregated mCherry-positive and mCherry-negative cells
216 in the CV condition (Figure 4E). The top upregulated genes in aggregated mCherry-positive cells
217 (*ctsbb*, *lrp2b*, *ctsl.1*, *dab2*, *cpvl*, *cubn*, *tdo2b*, *lgmn*, *fabp6*, *sptbn5*) were also significant LRE
218 cluster markers (Figure S4A). On the other hand, the most upregulated genes in aggregated
219 mCherry-negative cells (*fabp2*, *chia.2*, *fabp1b.1*, *apobb.1*, *apoa4b.1*, *apoa1a*, *tm4sf4*, *afp4.1*,
220 *apoc2*, *apoc1*) were also significant anterior enterocyte cluster markers (Figure S4B). This
221 presumably reflects the high relative abundance of LRE and anterior enterocytes in the mCherry-
222 positive and mCherry-negative groups, respectively (Figure 4C). However, expression of the top
223 differentially expressed genes also clearly delineated mCherry-positive and mCherry-negative
224 cells in secretory cell clusters, including goblet, EEC and acinar cells (Figure 4F, S4C-D).
225 Differential expression of these genes between mCherry-positive and negative cells was
226 significant in these clusters (Supplementary Table D). Upregulated genes in mCherry-negative
227 cells were highly enriched in anterior enterocytes and mCherry-negative cloaca 3, acinar, pharynx
228 and *best4*/*otop2* cells (Figure S4D). These data suggest that intact protein uptake in non-LRE
229 cells is associated with the expression of a subset of markers involved in protein uptake in LREs.
230
231 **Regional expression patterns and responses to the microbiome in LRE clusters**
232 Despite similarities between LREs and mCherry-positive cells from other clusters, LREs
233 maintained distinct transcriptional patterning that distinguished them from other cell types,
234 including close clusters (Figure 5A). For example, KEGG pathway analysis confirmed that the

lysosome pathway was strongly upregulated in anterior and posterior LREs in both GF and CV conditions (S5A–S5D), distinguishing them from their closest cluster neighbors (Figure 5B, S5E). In addition, both anterior and posterior LREs strongly expressed their characteristic endocytic machinery, composed of *cubn*, *dab2* and *amn* (Figure S5F).

Anterior and posterior LREs were distinguished by some notable differences in their transcriptional programs. Anterior LREs shared more transcriptional similarities to ileocytes than did posterior LREs. Bile salt transport genes, fatty acid binding protein (*fabp6*) and solute carrier family 10 member 2 (*slc10a2*), were highly expressed in ileocytes, but expression also occurred in the LRE clusters at a gradient from anterior to posterior LREs (Figure 5C–D). Further evidence of shared expression patterns between ileocytes and anterior LREs can be seen in their expression of tryptophan metabolic genes. Tryptophan metabolism was a significantly upregulated KEGG pathway in anterior LREs in the GF and CV conditions (Figure S5A-S5B). Expression of tryptophan metabolic genes, including kynurenine 3-monoxygenase (*kmo*) and tryptophan 2,3-dioxygenase a (*tdo2a*), occurred in LREs and ileocytes (Figure 5D–E). Anterior LREs showed high expression of tryptophan metabolic genes (*tdo2b*, *aldh9a1a.1*, *kmo*, *tdo2a*, *ddc*) in the GF and CV conditions (Figure S5G–S5H). Furthermore, anterior and posterior LREs were distinguished by differential expression of several peptidases (Figure S5I).

Several genes were differentially expressed between GF and CV conditions in the anterior and posterior LREs (S5J-S5K) (Supplementary Table E). The differences between the GF and CV conditions were most apparent in posterior LREs where expression of several peptidase genes was higher in GF than in CV larvae (Figure 5F). Carboxypeptidase vitellogenic like (Cpvl), a serine carboxypeptidase, and Cathepsin La (Ctsla), a cysteine-type peptidase, are predicted to localized to lysosomes (Mahoney et al. 2001; Tingaud-Sequeira and Cerdà 2007). Peptidase M20 domain containing 1, tandem duplicate 2 (Pm20d1.2) is an amino acid hydrolase (Long et al. 2016). These results raise the possibility that higher expression of protein-degradation genes *cpvl, ctsla* and *pm20d1.2* contributes to the faster degradation rates we observed in GF LREs.

In the CV condition, posterior LREs upregulated the expression of several genes involved in the immune response to bacteria (Figure 5G). These include genes for several proteins that mediate the immune response to toll-like receptor signaling from bacteria, including *LPS-responsive beige-like anchor protein* (*lrba*), *myeloid differentiation factor 88* (*myd88)*, and *hsp90b1* (Karmarkar and Rock 2013; Gibson et al. 2008; Franzenburg et al. 2012; van der Sar et al. 2006; Graustein et al. 2018; Wang et al. 2019). MyD88 signaling helps to prevent bacterial overgrowth and clears intestinal pathogens (Van Der Vaart et al. 2013; Karmarkar and Rock 2013; Gibson et al. 2008; Franzenburg et al. 2012; van der Sar et al. 2006). MyD88 also regulates expression of *JunD proto-oncogene, AP-1 transcription factor subunit* (*jund*), a LPS-sensor that can induce inflammation in response to the intestinal bacteria, including *Aeromonas* spp. (Meixner et al. 2004; Li et al. 2022). *EH-domain containing 1b* (*ehd1b*) is upregulated in response to bacterial infection and is involved in vesicle-mediated transport (Dubytska et al. 2022). These patterns suggest that the microbiome stimulates posterior LREs to upregulate expression of genes involved in directing the immune response to intestinal bacteria.

The microbiome also stimulated expression of dopamine synthesis and signaling genes in posterior LREs (Figure 5H). These include *dopamine decarboxylase* (*ddc*), which decarboxylates tryptophan to synthesize dopamine and serotonin (Koyanagi et al. 2012). Expression of *GNAS complex locus* (*gnas*), which is involved in the dopamine receptor signaling pathway (Lu et al. 2006; Vortherms et al. 2006), was also elevated in CV posterior LREs. Interestingly, posterior LREs were the only cell cluster in which *gnas* and *ddc* expression was

281 significantly higher in the CV than GF condition. These results suggest that the gut microbiome
282 increases dopamine synthesis and signaling pathways in posterior LREs.
283 The microbiome also upregulated several genes related to iron ion transport and
284 homeostasis in LREs (Figure 5I). In the CV condition, posterior LREs cells had significantly
285 elevated levels of *solute carrier family 11 member 2* (*slc11a2*), *ferroportin* (*slc40a1*), and
286 *melanotransferrin* (*meltf*) (S5K). Anterior LRE cells also showed increased expression of *slc40a1*
287 and *meltf* (Figure S5K). Slc11a2 helps regulate the influx of iron into the cell, while ferroportin
288 regulates the export of iron out of the cell (Yilmaz and Li 2018; Bao et al. 2024). Melanotransferrin
289 has iron-binding properties and is predicted to localize to the plasma membrane, where it
290 transports iron into the cell (Sekyere et al. 2006; Dunn, Rahmanto, and Richardson 2007).
291 Interestingly, melanotransferrin was an important cluster marker in Cloaca 3, a cell cluster that
292 only occurred in the CV condition and is directly adjacent to LREs in the intestine (Figure S3D).
293 These results suggest that upregulation of iron transport genes is a consistent response to
294 microbiome in LREs and other epithelial cells in the distal intestine.
295 Together, these scRNA-seq data revealed that LREs upregulate genes in response to
296 microbial colonization that are involved in innate immunity, iron homeostasis and dopamine-
297 synthesis and signaling pathways, and they downregulate several peptidases that may linked to
298 reduced protein degradation upon microbial colonization.
299
300 **Individual strains of microbes differentially affect LRE activity**
301 We next investigated if specific bacteria alter LRE kinetics and gene expression patterns.
302 To this end, we turned to monoassociation experiments (Pham et al. 2008), where larvae are
303 colonized with a single strain of bacteria at 3 dpf rather than the unfractionated microbiome used
304 to colonize CV fish.
305 We started by testing if commensal bacterial strains isolated from zebrafish gut
306 microbiomes (Stephens et al. 2016; Roeselers et al. 2011) were sufficient to reduce LRE protein
307 uptake kinetics. To address this question, we measured mCherry uptake in larvae reared either
308 as GF or monoassociated by a single strain, including *Acinetobacter calcoaceticus* ZOR0008,
309 *Aeromonas caviae* ZOR0002, *Vibrio cholerae* ZWU0020 or *Pseudomonas mendocina* ZWU0006
310 (Stephens et al. 2016). At 6 dpf, larvae were gavaged with mCherry (1.25 mg/mL), then mCherry
311 uptake was measured at 1 hour PG (Figure 6A). Interestingly, we found that while mCherry
312 uptake was only minimally reduced by *A. calcoaceticus* and moderately reduced by *P. mendocina*
313 and *A. caviae*, colonization with *V. cholerae* reduced mCherry uptake severely (Figure 6B).
314 Next, we investigated the mechanisms by which *V. cholerae* reduced mCherry uptake in
315 LREs. *V. cholerae* monoassociation did not significantly affect fish growth (Two-tailed T-test, $p =$
316 0.66, $n = 18 – 22$) (Figure S6A), suggesting that interactions with LREs rather than systemic effects
317 reduced uptake activity. To test if *V. cholerae* exposure induced acute effects on LRE uptake
318 activity, we gavaged GF larvae with live *V. cholerae* or PBS. Thirty minutes after initial exposure,
319 the larvae were gavaged again with mCherry (1.25 mg per mL). Interestingly, there was no
320 difference in mCherry uptake between larvae that were initially gavaged with live *V. cholerae* or
321 PBS (Figure S6A), indicating that longer-term exposure to *V. cholerae* is required to reduce
322 protein uptake activity in LREs. We next tested if *V. cholerae* monoassociation or CV conditions
323 increased the rate of transcytosis in LREs, which could lead to reduced mCherry signal in LREs.
324 To investigate this possibility, we gavaged GF, CV and *V. cholerae*-monoassociated larvae with
325 mCherry (1.25 mg/mL) and then measured the mCherry signal in the pronephros at 4 hours PG.
326 There was no difference in pronephros signal between these conditions, indicating that intestinal
327 microbes were not causing LREs to increase mCherry trans-epithelial transport through

transcytosis (Figure S6B). Finally, we tested if *V. cholerae* lowered mCherry uptake in LREs by reducing its concentration in the intestinal lumen, perhaps by promoting intestinal motility (Wiles et al. 2020; Logan et al. 2018). To do so, we analyzed confocal images of GF and *V. cholerae*-colonized larvae taken at one hour PG and measured luminal mCherry concentration in the intestinal lumen proximal to LREs. The concentration was the same in both conditions (Figure S6C), showing that *V. cholerae* does not significantly reduce mCherry concentrations in the intestinal lumen within these timeframes.

Our monoassociation experiments suggested that microbes selectively affect LRE activity. To investigate if this effect is mediated by transcriptional regulation of specific protein uptake and degradation machinery genes, we employed quantitative hybridization chain reaction (HCR) RNA-FISH (Choi et al. 2018) to compare expression of target genes between GF and monoassociated larvae. We focused on *dab2* and *cubn*, which encode endocytic components critical for the LRE's ability to internalize proteins and soluble cargoes (Park et al. 2019).

Similar to what we found previously using conventional in situ hybridization probes (Park et al. 2019), the *dab2* HCR probe was highly specific to LREs and pronephros (Figure 6C). By comparing the integrated signal obtained from max projection of confocal stacks, we found that GF larvae had significantly higher levels of *dab2* expression than those colonized with *V. cholerae* (Figure 6D). Interestingly, the *dab2* expression profiles in GF and *V. cholerae*-colonized larvae showed patterns reminiscent to those of mCherry uptake, with a peak in the anterior LREs that tapers off in the posterior LREs (Figure 6D). Since mCherry uptake is dependent on Dab2 (Park et al. 2019), this pattern may help explain why mCherry uptake tends to peak in the anterior LREs.

Next, we tested the effects of these strains on *cubn* expression. Similarly to *dab2*, the *cubn* HCR probe highlighted LREs and showed faint fluorescence in pronephros (Figure 6E). We found that while *V. cholerae* significantly reduced *cubn* expression, *A. calcoaceticus* did not (Figure 6F). These patterns are consistent with the degree to which *V. cholerae* and *A. calcoaceticus* affected mCherry uptake in LREs (Figure 6B). Interestingly, the *cubn* expression profile in LREs was different from *dab2*. It lacked an anterior peak, suggesting that *cubn* expression is perhaps more uniform throughout the LREs (Figure 6F).

In addition to the endocytic machinery, we also tested the effects of individual microbial strains on the expression of LRE-enriched proteases *ctsh* and *ctsz*. Our scRNA-seq data showed that these peptidases are highly upregulated in GF LREs. We found that *V. cholerae* reduced expression of *ctsh* and *ctsz* compared to *A. calcoaceticus* and GF larvae, which presented similar levels of *ctsz* expression (Figure 6G–6H).

Together, our data reveal that microbial colonization reduces both protein uptake and degradation in LREs by modulating the expression of endocytic and lysosomal proteins. Our data also suggest that LREs have functional heterogeneity, which may represent some degree of specialization into two different clusters as suggested by the scRNAseq data.

LRE activity impacts the gut microbiome in a diet-dependent manner

We next investigated whether LRE activity has reciprocal effects on the gut microbiome. Our previous research demonstrated that *cubn* mutants have significantly reduced survival compared to heterozygotes when they are fed a low protein diet from 6 to 30 dpf (Park et al. 2019). We hypothesized that the combination of the *cubn* mutation with a low protein diet fostered a microbial community that further reduced the host's protein uptake capabilities.

To explore this possibility, we tested the combined effects of the *cubn* mutation and custom-formulated, isocaloric high and low protein diets (see Materials and Methods) on the larval zebrafish microbiome. We fed high-protein (HP) or low-protein (LP) diets to *cubn* heterozygote

375 and homozygous mutant siblings from 6 to 30 dpf, then performed 16S rRNA gene sequencing
376 on whole larvae to identify microbial populations (Figure 7A). Initial analyses highlighted that
377 zebrafish larvae developed bacterial communities that were distinctly different from the diets and
378 tank water (Bray Curtis distance, p = 0.0001) (Figure S7A). Larval microbiomes from different
379 tanks were not significantly different in either HP (Bray Curtis distance, p = 0.08) or LP-fed (Bray
380 Curtis distance, p = 0.13) conditions (Figure S7B). Diet strongly affected microbiome composition
381 in heterozygotes (Bray Curtis distance, p = 0.001), but not in *cubn* homozygous mutants (Bray
382 Curtis distance, p=0.18) (Figure 7B-C). Mutants had significantly different microbiomes than
383 heterozygotes when they were fed a LP diet (Bray Curtis distance, p = 0.023), but not a HP diet
384 (Bray Curtis distance, p = 0.34) (Figure 7B-C). In contrast, beta dispersion was not significantly
385 different between HP or LP-fed *cubn* heterozygotes and mutants (Bray Curtis dispersion, p = 0.24)
386 (Figure S7C) (Zaneveld, McMinds, and Thurber 2017). Some of these effects may reflect
387 differences in taxonomic richness, which was significantly impacted by genotype and diet (1-way
388 ANOVA, p = 0.042) (Figure 7D). LP-fed *cubn* mutants had significantly lower microbial richness
389 than HP-fed mutants (Two tailed t-test, p= 0.0094, n = 6 - 9). These results suggest that the
390 combination of the LP-diet and *cubn* mutation lowers taxa richness and affects the mutant
391 microbiome.
392 The broad differences in microbiome diversity led us to investigate class and genus-
393 level effects of the *cubn* mutation and LP diet on the microbiome. The effects of dietary protein
394 on the microbiome were clearly seen at the class level (Figure 7E). Gammaproteobacteria were
395 significantly more abundant in HP than LP-fed heterozygotes (DESeq2, padj = 0.02). LP-fed
396 mutants were deficient in Alphaproteobacteria, which were more abundant in LP-fed
397 heterozygotes (DESeq2, padj = 0.021) (Figure 7E). Indeed, one important trend was that mutants
398 consistently had fewer differentially abundant taxa than heterozygotes at the class and genus
399 levels (Figure 7F). The few taxa that were more abundant in mutants than heterozygotes emerged
400 when they were fed the LP diet (Figure 7F).
401 The impacts of dietary protein and the *cubn* mutation on the microbiome were also
402 apparent at the genus level (Figure 7F–7G) (Supplementary Table F). *Pseudomonas* spp. were
403 significantly more abundant in HP than LP-fed heterozygotes (DESeq2, padj = 0.002) (Figure
404 7G). One genus, *Hassalia*, was significantly more abundant in LP-fed mutants than in
405 heterozygotes (DESeq2, padj = 6.04E-21). Independently of diet, *Aeromonas* spp. were more
406 highly abundant in *cubn* mutants than heterozygotes (DESeq2, padj = 0.01) (Figure 7H).
407 Interestingly, our monoassociation experiments demonstrated that a member of *Aeromonas*
408 genus, *A. caviae*, can reduce protein uptake activity in LREs (Figure 6B).
409 Together, these results suggest that LRE activity and dietary protein content can
410 interactively affect the larval zebrafish microbiome. The combination of the LP diet and *cubn*
411 mutation cause a less rich microbiome to develop. Furthermore, the *cubn* mutation may lead to
412 the proliferation of certain microbes that can reduce protein uptake activity in LREs.
413
414 **DISCUSSION**
415
416 The results of our investigations reveal reciprocal interactions between LREs and the gut
417 microbiome that impact host nutrition. We show that the gut microbiome slows the rates of protein
418 uptake and degradation in LREs and reduces expression of lysosomal protease genes. We also
419 found that monoassociated bacteria such as *Aeromonas* and *Vibrio cholerae* reduce protein
420 uptake in LREs and downregulate expression of endocytic and protease genes. Finally, we show
421 that impaired LRE protein uptake activity and dietary protein content impact the microbiome.

Precise delivery of fluorescent cargoes to the gut via gavage provided a quantitative assay that allowed us to uncover that the gut microbiome reduces the rate of cargo uptake and protein degradation in LREs. These effects were caused by microbially-induced metabolic effects in the LREs, not quantity of LREs that developed or the availability of luminal protein. The significance of the microbe dependent downregulation of protein uptake remains unclear. One possibility is that this effect limits the transepithelial transport of microbial products, which occurs as a byproduct of the endocytic activity of LREs, thus dampening the expression of pro-inflammatory markers. This microbial suppression of the principal physiologic function of LREs (i.e., protein uptake and degradation) is strikingly similar to the microbial suppression of genes involved in lipid absorption in enterocytes within small intestine of zebrafish (Camp et al. 2012; Willms et al. 2022) and mice (Camp et al. 2014). This suggests that microbial inhibition of absorptive gene expression programs across enterocyte populations may be a broader conserved theme in intestinal physiology.

Recent scRNA-seq studies suggested that the gut microbiome affects the transcriptome of LREs and other ileal cell types in zebrafish by upregulating expression of immune markers (Massaquoi et al. 2023; Jones et al. 2023; Willms et al. 2022). Our dataset also showed that microbes upregulated expression of immune markers in LREs. However, the immune markers that other studies attributed to LREs were not upregulated by LREs in our dataset. For example, we found that several of these immune markers (*saa, prdx1, lect2l)* were actually upregulated in cloaca cells, not LREs (Willms et al. 2022). These misalignments could result from previous datasets including relatively few LREs that were over-clustered with cloaca, pronephros or other ileal cells. Furthermore, these studies did not functionally evaluate intestinal protein absorption, making it difficult to assess the impact of microbes on LRE-dependent processes. Sequencing FACS-sorted IECs minimized contamination from other tissues like the pronephros. Furthermore, we captured a larger number of bona fide LREs from GF and CV larvae that were positively identified in our dataset by their fluorescent label and transcriptional program. Thus, our single cell dataset provides a high degree of resolution into the effects of the microbiome on LREs and IECs and made it possible to differentiate anterior from posterior LREs.

Labeling intestinal cells by mCherry gavage allowed us to identify all intestinal cells that take up luminal protein, including EECs, goblet and acinar cells. These cells showed greater expression of LRE markers than mCherry-negative secretory cells. Unlike LREs, they do not appear to play a significant role in protein absorption as gavaging with DQ Red BSA, which labels cells with lysosomal degradation activity, did not label these cells. Remarkably, anterior enterocytes and *best4/otop2* cells were completely mCherry-negative, indicating that they are virtually devoid of endocytic activity.

The proportion of mCherry-positive secretory cells was greater in the CV condition. EECs are known for sensing intestinal nutrients (Goldspink, Reimann, and Gribble 2018), but they also influence the intestinal inflammation response to the gut microbiome (Worthington, Reimann, and Gribble 2018). Intestinal microbes, including *Acinetobacter*, regulate EEC signaling activity in zebrafish larvae (Ye et al. 2019). In the mouse intestine, some EECs have a synaptic connection to neurons through neuropods (Bohórquez et al. 2015), which could facilitate the uptake of mCherry by neurons that we detected. Neuronal expression of *cldn15la* was detected in our data and other datasets (Willms et al. 2022; Sur et al. 2023), allowing them to be captured by our cell sorting here. Goblet cells secrete a mucous barrier that protects the intestinal epithelium from microbial infection (Belkaid and Hand 2014). They also sample luminal antigens and endocytose luminal cargoes as a byproduct of membrane recycling (Birchenough et al. 2015; Mcdermott and Huffnagle 2014). Similarly, acinar cells secrete digestive enzymes and antimicrobial peptides into

469 the intestinal lumen (Yee, Lorent, and Pack 2005; Ahuja et al. 2017). The gut microbiome may
470 stimulate mucin production and the exocytosis of antimicrobial peptides, which would cause these
471 cells to upregulate their compensatory endocytic activity and lead to mCherry uptake. We
472 speculate that the mCherry uptake we observed in these non-LRE cell types could be related to
473 these respective known functions.

474 The overwhelming majority of LREs were mCherry-positive regardless of microbial
475 colonization. This result aligns with our kinetic assays, which showed that LREs have protein
476 uptake activity in both GF and CV conditions. However, our gavage assays showed that anterior
477 LREs in the GF condition took up protein more rapidly than they did in the CV condition. However,
478 the anterior LREs accumulate more protein than posterior LREs in both the GF and CV conditions.
479 The high uptake activity in this anterior LRE region may be due to greater expression of *dab2*,
480 which our HCR results support. Thus, the anterior LRE region has a greater dynamic range in
481 protein uptake activity, and that may partially explain why the effect of the microbiome was more
482 apparent in this region. In addition, anterior LRE protein uptake activity may have remained more
483 active than posterior LREs in both GF and CV conditions due to reduced expression of innate
484 immune factors compared to posterior LREs. Through high rates of apical endocytosis, LREs
485 could be exposed to large amounts of microbial antigens. Posterior LREs upregulated
486 inflammatory response genes in the CV condition, but anterior LREs did not. Furthermore, anterior
487 LREs showed higher expression of tryptophan metabolism genes than posterior LREs, which may
488 attenuate their inflammatory response to the microbiome. Tryptophan metabolites, including
489 kynurenine derivatives, are AhR receptor ligands that downregulate host immune response to
490 bacterial antigens (Bessede et al. 2014). However, tryptophan metabolism may be an important
491 microbiome-tolerance pathway in both LRE regions. The microbiome induced expression of *haao*,
492 an enzyme that produces kynurenine metabolites (Xue et al. 2023), in posterior LREs. These
493 results suggest that tryptophan metabolic activity in LREs could participate in host tolerance of
494 the gut microbiome, and inflammation may affect protein uptake activity in LREs

495 LREs may play a role in shaping the gut microbiome community by impacting luminal iron
496 levels. Microbes strongly upregulated expression of iron-ion transport genes in LREs that control
497 the influx and efflux of cellular iron. The microbiome increases intestinal iron absorption
498 (Mayneris-Perxachs, Moreno-Navarrete, and Fernández-Real 2022), but its effect on iron
499 absorption in LREs is unknown. Host iron nutrition and luminal iron levels can affect the gut
500 microbiome community and proliferation of microbial pathogens (Mayneris-Perxachs, Moreno-
501 Navarrete, and Fernández-Real 2022; Dostal et al. 2012). Iron absorption and secretion by LREs
502 may affect the gut microbiome community and play a role in host-microbiome homeostasis.

503 The impact of intestinal microbes on LRE activity may be dependent on their inflammatory
504 properties. Monoassociating larvae with *A. calcoaceticus*, *P. mendocina*, *V. cholerae*, and *A.*
505 *caviae* produced differential effects on protein uptake activity and expression of endocytic
506 machinery. *A. calcoaceticus* may be classified as an anti-inflammatory bacteria because it
507 reduces intestinal neutrophil recruitment (Rolig et al. 2015). Colonization with *A. calcoaceticus*
508 only mildly reduced protein uptake activity, and it did not reduce expression of endocytic
509 machinery. In contrast, the pro-inflammatory strains, *V. cholerae* and *A. caviae* (Rolig et al. 2015),
510 reduced LRE activity and endocytic expression. *V. cholerae* colonization causes intestinal
511 neutrophil recruitment and stimulates macrophages to express TNF-alpha (Wiles et al. 2020; Ngo,
512 Amitabh, Sokoloff, Trinh, Wiles, Guillemin, and Parthasarathy 2024). Importantly, the *V. cholerae*
513 strain we used here does not encode cholera toxin or toxin-coregulated pilus (Stephens et al.
514 2016). This strain has been shown to increase intestinal contractility in zebrafish (Ngo, Amitabh,
515 Sokoloff, Trinh, Wiles, Guillemin, Parthasarathy, et al. 2024) and may affect protein absorption

under nutrient limiting conditions. However, in our gavage assays the luminal protein concentrations are never limiting and were not affected by *V. cholerae* colonization (Fig. S6D). Future studies could identify the underlying bacterial signals causing LREs to regulate protein uptake activity and host signal transduction mechanisms.

Our investigations into the impact of LRE protein uptake activity on the gut microbiome revealed diet-dependent effects on the microbial community. LP-fed, *cubn* mutants developed a distinct microbiome community with diminished species richness. *Aeromonas* was the only genus that proliferated in *cubn* mutants compared to heterozygotes. While *Aeromonas* is considered a part of the core zebrafish gut microbiome (Roeselers et al. 2011), some species are inflammatory (Rolig et al. 2015). As discussed, *A. caviae* can reduce LRE protein uptake activity. This result suggests that host protein deprivation through the impaired LRE activity may lead to proliferation of proinflammatory bacteria like *Aeromonas* that can further reduce protein uptake activity by LREs.

Altogether, our results show reciprocal regulation between LREs and the gut microbiome, along with the impact of the gut microbiome on protein uptake by IECs. These results pave the way to identify microbial signals or antigens that reduce protein uptake activity by LREs. Future studies could characterize the effect of microbes on protein-uptake by secretory cell populations. Further investigations into the tryptophan metabolism, iron ion transport, and expression of bacteria-sensing genes by LREs could reveal mechanisms for host-microbiome homeostasis.

Acknowledgements

We thank Dan Levic and Carina Block for critical reading of our manuscript, Colin Lickwar for helpful advice on bioinformatic analysis, Jia Wen for advice on monoassociation, Akankshi Munjal for advice on HCR, the Duke ZeCore for fish care, Duke Microbiome Core for assistance with 16S rRNA gene sequencing, and the Duke Center for Genomic and Computational Biology for help with scRNA sequencing. This work was funded by NIH grants DK132120 to M.B. and DK121007 to M.B. and J.F.R.

METHODS

Fish

The Duke University Institutional Animal Care and Use Committee (IACUC) guidelines were followed in the care and use of all fish in this project. We maintained zebrafish (*Danio rerio*) stocks on a recirculating system at 28˚C with a controlled, 14-hour light and 10 hour dark cycle (Westerfield 2000). Breeding adult zebrafish were fed a 1:1 ratio of GEMMA Micro (Skretting) and artemia. To breed fish, males and females were placed in mating tanks with dividers overnight, and dividers were removed the following morning. Zebrafish from the Ekkwill (EK) background between 6 – 30 dpf were used in this study.

Gnotobiotic zebrafish husbandry

Previously described gnotobiotic husbandry methods were used to raise GF, CV, and monoassociated larvae (Pham et al. 2008). Briefly, embryos were treated with antibiotic zebrafish media, followed by iodine and bleach washes to eliminate microbes from their chorions at 0 dpf. Following microbe-removal steps, embryos were housed in sterile cell culture flasks containing autoclaved gnotobiotic zebrafish media (GZM) and incubated at 28˚C. Each flask contained 30 embryos in 30 mL media. At 3 dpf, gnotobiotic larvae were either conventionalized, monoassociated, or remained in the GF condition. In this process, 80% of the media was

563 replaced. The media in GF and monoassociated flasks was replaced with 24 mL autoclaved GZM,
564 while CV flasks received 12 mL autoclaved GZM and 12 mL 5 µm-filtered zebrafish system water.
565 After this step, gnotobiotic zebrafish either (Protocol A) continued to be raised as described (Pham
566 et al. 2008), or (Protocol B) they were raised by our modified protocol designed to boost the
567 bacterial load. In Protocol A, each flask was given 100 µL ZM000 daily from 3 – 5 dpf following
568 media changes, and 80% of the media was replaced with autoclaved GZM from 4 – 5 dpf. In
569 Protocol B, flasks are given 150 µL ZM000 from 3 – 5 dpf, and 40% of the media was replaced
570 with autoclaved GZM from 4 – 5 dpf. The scRNA-seq (Figure 3 – 5), lucifer yellow gavage (Figure
571 1G), and long-term mCherry gavage (Figure 1D – E) larvae were raised according to Protocol A.
572 The larvae used in rapid mCherry-uptake (Figure 1B – C), mTurquoise degradation (Figure 2),
573 and monoassociation (Figure 6) experiments were raised according to Protocol B. At the 6 dpf
574 endpoint, GF flasks were tested for sterility by spot-testing on TSA plates, as well as brain-heart,
575 dextrose and nutrient broth. The bacterial density in CV and monoassociated media was tested
576 by serial dilutions on TSA plates. Zebrafish larvae were monoassociated with *Acinetobacter*
577 *calcoaceticus* ZOR0008, *Aeromonas caviae* ZOR0002, *Vibrio cholerae* ZWU0020 or
578 *Pseudomonas mendocina* ZWU0006 that were previously isolated from conventionally-reared
579 zebrafish (Stephens et al. 2016). Bacteria stocks used in monoassociation were kept in 50%
580 glycerol at -80˚C for long term storage and on tryptic soy agar (TSA) plates at 4˚C for short term
581 storage. Bacteria were cultured by incubating picked colonies in LB liquid media on a shaker table
582 at 30˚C for 24 – 72 hours to reach turbidity with an OD600 of 1 – 3. Cultures were re-suspended
583 in 1X PBS after spinning at 5,000 RPM for 2 minutes. The bacterial density (CFU/mL) was
584 determined by plating serial dilutions on TSA plates and incubating overnight at 37˚C. Re-
585 suspended bacteria was added to GF flasks to colonize larvae at 3 dpf. For the mCherry gavage
586 experiment (Figure 6B), GF larvae were colonized with approximately 6 x 10^8 CFU of *V. cholerae*,
587 *A. caviae*, *P. mendocina*, or *A. calcoaceticus*. The final bacterial density in the media was
588 measured by plating serial dilutions on TSA plates.
589
590 **Fluorescent protein purification**
591 Previously described methods were used to prepare mCherry and mTurquoise (Park et al.
592 2019).
593
594 **Gavage assays**
595 *Gavage*
596 Larvae were sedated with 0.22 µm-filtered 1X Tricaine (0.2 mg/mL). Sedated larvae were
597 suspended in 3% methyl cellulose and gavaged with 4 nL of fluorescent cargo (Cocchiaro and
598 Rawls 2013). Larvae were placed in a zebrafish incubator to absorb the fluorescent cargo
599 following gavage.
600
601 *Rapid uptake*
602 Larvae were gavaged with mCherry (1.25 mg/mL), then incubated briefly. After designated time
603 intervals (5 – 40 minutes) post gavage (PG), mCherry was cleared from the intestinal lumen by
604 gavaging larvae with 1X PBS. Following clearance, larvae were immediately preserved in 4%
605 PFA in PBS. Samples were stored at 4˚ C overnight. The following day, larvae were mounted on
606 glass-bottomed dishes and imaged by confocal microscopy.
607 Fluorescence profiles of mCherry uptake in LREs were generated by analyzing confocal
608 images in ImageJ (version 1.53t). Images were z-projected as max intensity plots. The LRE region
609 was delineated with a rectangular selection tool to generate plot profiles of mCherry fluorescence

along the LRE region. The anterior LRE region was designated as the 50 - 150 μm region flanking peak fluorescence at 60 minutes PG. A 100 μm segment length was chosen because it encompasses approximately one third of the LRE region. In this experiment, the 50 – 150 μm position was selected because peak fluorescence occurred at approximately 100 μm, so analysis covers the most kinetically active LREs. The posterior LRE region was designated as the 100 μm region immediately distal to the anterior region (150 – 250 μm).

mCherry fluorescence in anterior versus posterior LREs was calculated from area under the curve (AUC) measurements (Figure S1A – S1B). The average AUC measure at each time point was calculated. These values were normalized by dividing them by the peak AUC value at 60 minutes post gavage in the GF condition. The regional differences in mCherry fluorescence between anterior and posterior LREs from 5 – 60 minutes post gavage was calculated with a 2-way ANOVA with Bonferroni's multiple comparisons.

The rate of mCherry accumulation in anterior LREs (Figure S1C) was calculated next. The average and standard error in mCherry fluorescence at each time point was calculated for GF and CV conditions. These were normalized when they were divided by the maximum average value, which occurred in the GF condition at 60 minutes PG. A simple linear regression was used to calculate the difference in the mCherry-accumulation slopes between GF and CV conditions.

Long term uptake of mCherry (1 – 5 hours PG)

Following mCherry gavage (1.25 mg/mL), larvae were incubated, then preserved in 4% PFA at designated time intervals (1 – 5 hours PG). Samples were stored at 4˚C overnight, then imaged by confocal microscopy. Confocal images were analyzed with ImageJ. The same protocol was used to process images. To compare mCherry and Lucifer yellow uptake in the whole LRE region, the average fluorescence and standard error were calculated for each 30 μm LRE segment in GF and CV conditions (Figure 1D-F). The difference in fluorescence profiles between GF and CV conditions at each time point was then calculated with a 2-way ANOVA. To do so, the average fluorescence in each segment (30 μm) of the LRE region (300 μm) was compared between the GF and CV conditions.

To compare the rate of mCherry uptake in anterior LREs, the average fluorescence and standard error were calculated for the 0 – 100 μm segment in GF and CV conditions. A simple linear regression calculated the difference in mCherry-uptake rate between conditions, along with the difference in slope from zero. A 100 μm segment length was chosen because it encompasses approximately one third of the LRE region. In this experiment, the 0 – 100 μm position was selected because peak fluorescence occurred at approximately 50 μm, so analysis covered the most kinetically active LREs.

Lucifer yellow uptake

Larvae were gavaged with 4 nL of Lucifer yellow (1.25 mg/mL), then incubated. Immediately before imaging, luminal Lucifer yellow was cleared with a 1X PBS gavage. Larvae were live imaged to avoid signal quenching by PFA. The same protocol was used to process these images as mCherry-gavaged larvae. To compare Lucifer yellow uptake in the whole LRE region, the average fluorescence and standard error were calculated for each 50 μm LRE segment in GF and CV conditions. The difference in fluorescence between GF and CV conditions at each time point was then calculated with a 2-way ANOVA. The same statistical methods were used to calculate the 2-way ANOVA as the long-term mCherry uptake experiments.

mTurquoise degradation

657 Larvae were gavaged with mTurquoise (25 mg/mL) and incubated for 1 hour. Luminal mTurquoise
658 was cleared with a 1X PBS gavage. Sedated larvae were mounted on glass-bottom plates and
659 live imaged by confocal microscopy from 20 – 60 minutes post clearance.
660 mTurquoise fluorescence was quantified in the whole LRE region using ImageJ as
661 described above. Live imaging allowed us to track mTurquoise degradation over time in individual
662 fish. The maximum mTurquoise fluorescence value for each individual fish was calculated at the
663 first time point (20 minutes). All mTurquoise fluorescence measures for each respective fish were
664 then divided by the fish's maximum value, effectively converting mTurquoise fluorescence
665 measures to a 0 – 100% scale across all time points. After that, we calculated average
666 mTurquoise fluorescence in individual fish at each time point and normalized to the fish's average
667 value at 20 minutes PG. Next, we generated a degradation curve by finding the mean and
668 standard error across fish from GF or CV conditions. These values were linearized when we
669 transformed the x-axis by dividing 1 by the time point (i.e., the x-axis value for the 20-minute time
670 point would be 1/0.333 or 3). Finally, we calculated the difference in degradation rate between
671 GF and CV larvae with a simple linear regression.
672
673 **Microbial degradation of mCherry**
674 We tested if the larval zebrafish microbiome can degrade mCherry. CV larvae (n = 27) were
675 anesthetized with 0.22 µm-filtered Tricaine, then homogenized in GZM with a Tissue-Tearor™
676 (BioSpec Products, inc., model # 985370). The homogenate was spun at 5,000 RPM for 2 minutes
677 and re-suspended in 1X PBS. mCherry was added to the zebrafish microbiome mixture and the
678 1X PBS control (25 µg/mL). The microbiome and control were added to a 96 well plate. The
679 mCherry fluorescence was measured in each well periodically over 2 hours. Average mCherry
680 fluorescence (AU) over time was compared between treatments with a simple linear regression.
681
682 **Trans-epithelial transport**
683 GF and CV larvae were anesthetized with 1X Tricaine at 6 dpf. Then, anesthetized larvae were
684 gavaged with mCherry protein (1.25 mg/mL). Larvae were placed in a 28˚C incubator to absorb
685 the mCherry for 4 hours. At that point, larvae were fixed in 4% PFA and stored overnight at 4˚C.
686 Fixed samples were washed in 1X PBS three times before being mounted in 0.9% low-melt
687 agarose in egg water. Imaging was done with a 25X objective and resonant scanner, and images
688 were taken as z-stacks. Statistics were done by 1-way ANOVA with Tukey's multiple comparisons
689 test.
690
691 **LRE segmentation**
692 GF and CV larvae were anesthetized with 1X Tricaine at 6 dpf. Then, DQ-red BSA (50 µg/mL)
693 was gavaged into larvae until the whole gut was filled with the gavage mixture (4 nL). After 0.5
694 hours of uptake, the larvae were flushed with a 1X PBS gavage until no visible red color was
695 observed in the gut. Larvae were stored in a 28˚C incubator for 3 hours after DQ-red BSA gavage.
696 During this incubation period, DQ-red BSA fluorescence activated when the dye was catabolized
697 by lysosomal proteases, thus marking the lysosomal vacuole of each LRE. Larvae were then
698 anesthetized with 1X Tricaine, mounted in 1.3% low-melt agarose in egg water, and live imaged
699 by confocal microscopy. Imaging was done on a Leica SP8 microscope using a 25X objective
700 (Leica) and resonant scanner.
701 Images were imported into Ilastik version 1.3.3 and segmented by the Pixel Classification
702 program. The program is trained to identify DQ-red BSA-filled LRE vacuoles by machine learning
703 where 10 – 15 LRE vacuoles are manually marked per image. This process is carried out for 5 –

10 images before the program is allowed to train itself based on these manual feed-ins. Any errors made by the program are then manually corrected and used to improve the segmentation process. After the segmentation program is trained to have at least an estimated 85% accuracy, the results are exported as probability maps in .h5 format, which are then fed into Ilastik's Object Classification program. The following parameters are used for the classification process: Method: Hysteresis; Smooth: σ=1.0 for x-,y- and z-axis; Threshold: core=0.60, final=0.60; Don't merge objects. After checking the accuracy of object classification, the results are then exported as .cvs files from which the numbers of objects (in this case LRE vacuoles) are extracted. Statistics were done by 1-way ANOVA with Tukey's multiple comparisons test.

Fluorescence activated cell sorting for single cell RNA-sequencing

TgBAC(cldn15la-GFP)^{pd1034} larvae (Alvers et al. 2014) were raised in GF and CV conditions to 6 dpf as described above. These transgenic larvae express GFP in IECs. GF flasks were screened for sterility as described above. Bacterial density in CV flasks ranged from approximately 5 x 10^4 – 5 x 10^9 CFU/mL. In total, 276 CV and 277 GF, GFP-positive larvae were gavaged with mCherry (1.25 mg/mL) and incubated for 4 hours to mark LREs with mCherry in addition to GFP. Then, larvae were dissociated, and cell suspensions were sorted by FACS as described (Park et al. 2019). The cell death marker, 7AAD (5 µg/mL), was added to cell suspension prior to FACS to remove dead cells. Cells were sorted on a MoFlo Astrios EQ cell sorter (Beckman Coulter) by the Flow Cytometry Shared Resource Center (Duke University). In total, 61,000 double-positive and 156,000 GFP-positive cells were collected from GF larval samples. From CV larval samples, 51,000 double-positive and 140,000 GFP-positive cells were collected. Cells were collected in RLT Plus Buffer (Qiagen RNeasy Plus Micro Kit: QIAGEN Cat No. 74034) media.

To test mCherry-uptake activity in this cohort, GF and CV larvae were gavaged with mCherry (1.25 mg/mL) at the same time as larvae destined for scRNA-seq. These larvae were incubated for 5 hours, then preserved in 4% PFA. They were confocal imaged the following day as described above.

Single cell RNA-sequencing library preparation and sequencing

Immediately after cells were sorted, we began library preparation with the Chromium Next GEM Single Cell 3' GEM, Library & Gel Bead Kit v3.1 following the kit protocols. GEMS were stored at -20˚C for three days prior to post GEM-RT cleanup and cDNA amplification following the kit protocol. Quality control was done by measuring cDNA concentration and size distribution with the ScreenTape assay using the Agilent TapeStation. Libraries were submitted to the Duke Center for Genomic and Computational Biology for sequencing. They were sequenced on the Illumina NovaSeq 6000 platform with 100 bp paired-end reads. Sequencing results are deposited at NCBI Sequence Read Archive (BioProject Accession #: PRJNA1192682).

Single cell RNA-sequencing analysis

Cell Ranger v3.0 (10X Genomics) was used to demultiplex sequencing files and align reads to the zebrafish reference genome, Danio Rerio GRCz11. Analysis was performed in RStudio (version 2023.12.1) using the Seurat package (version 5.0.1). Reads were filtered by the following criteria: UMIs/cell > 500, genes/cell > 250, Log10GenesperUMI > 0.8, and mitoRatio < 0.5. The SCTransform method was used for normalization. Cells were clustered with a resolution of 0.5. Cluster markers were identified using Seurat's "FindMarkers" function. Cluster identity was determined by cross-referencing marker genes to other scRNA-seq and RNA-sequencing datasets (Park et al. 2019; Wen et al. 2021; Willms et al. 2022). After the LRE cluster was

751 identified, it was re-clustered with a resolution of 0.5 to form two sub-clusters. The GF and CV
752 objects were merged to form one Seurat object.
753
754 ***In Situ* Hybridization Chain Reaction (HCR)**
755 HCR probes, hairpins, amplification, wash and hybridization buffers were purchased from
756 Molecular Instruments (Choi et al. 2018). Our methods were adapted from a previously published
757 procedure for performing HCR on zebrafish embryos (Munjal et al. 2021). At 6dpf, larvae were
758 anesthetized and fixed in 4% PFA, then incubated on a shaker table for two hours. Larvae were
759 washed with 1X PBS twice, followed by two cold acetone washes. Larvae were incubated in cold
760 acetone at -20˚C for 8 minutes, followed by three 1X PBS washes. For the detection stage, larvae
761 were first incubated in probe hybridization buffer at 37˚C for 30 minutes on a shaker. Larvae were
762 incubated in probe solution (4 nM) on a shaker at 37˚C for 24 – 48 hours. Excess probes were
763 removed by washing larvae four times with preheated, 37˚C probe wash buffer, incubating
764 samples on a shaker table at room temperature for 15 minutes each time. This step was followed
765 by two, 5 – 10 min SSCT washes on a shaker at room temperature. For the amplification stage,
766 larvae were incubated in room temperature amplification buffer for 30 minutes. Hairpins (30 pmol)
767 were prepared by heating at 95˚C for 90 seconds, then snap-cooled in the dark at room
768 temperature 30 minutes. Hairpins were added to amplification buffer. Larvae were incubated in
769 the hairpin solution in the dark at room temperature overnight. Excess hairpins were removed
770 with five SSCT washes on a shaker table at room temperature. The duration of the first two
771 washes were 5 minutes, followed by two 30-minute washes and one 1-minute wash. Samples
772 were protected from light during the washes. Larvae were imaged by confocal microscopy using
773 a Leica SP8 microscope equipped with 10X and 25X objectives. The difference in HCR probe
774 fluorescence profiles between GF and monoassociated larvae was calculated with a 2-way
775 ANOVA. To do so, the average probe fluorescence in each segment (30 μm) of the LRE region
776 (300 μm) was compared between the GF and monoassociated conditions.
777
778 **High and low-protein diet feeding**
779 Sibling larvae from a *cubn* heterozygous-mutant cross were conventionally raised from 0 – 5 dpf.
780 At 6 dpf larvae were housed in 3 L tanks at a density of 10 larvae per tank and raised on our
781 standard circulating aquarium. From 6 – 30 dpf, larvae were fed 10 mg/day of a custom formulated
782 high (HP) or low-protein (LP) diet daily between 11 am – 12 pm. There were three tanks per diet.
783 Diet formulations are described in detail below.
784
785 **16S rRNA gene sequencing**
786 At 30 dpf, samples were collected for 16S rRNA gene sequencing. Larvae were anesthetized with
787 0.2 μm-filtered tricaine in autoclaved egg water. After the water was removed, larvae were flash
788 frozen in liquid nitrogen. Tank water samples were collected by passing 50 mL through a 0.2 μm
789 filter (Pall Corporation MicroFunnel Filter Funnels #4803), then flash freezing the filter paper in
790 liquid nitrogen.
791 Samples were put on dry ice during transport to the Duke Microbiome Shared Resource
792 for 16S rRNA gene sequencing. Larval DNA was extracted with the MagAttract PowerSoil DNA
793 EP Kit (Qiagen, 27100-4-EP). Following the Earth Microbiome Project protocol
794 (http://www.earthmicrobiome.org/), the V4 region was amplified by polymerase chain reaction
795 with the 515F and 806R primers, which are barcoded for multiplexed sequencing. PCR product
796 concentration was measured with the Qubit dsDNA HS assay kit (ThermoFisher, Q32854) on a
797 Promega GloMax plate reader. Equimolar PCR products from all samples were pooled and

sequenced with 250 bp PE reads on the MiSeq Illumina platform. Sequencing results are deposited at NCBI Sequence Read Archive (BioProject Accession #: PRJNA1188138).

Paired-end fastq files were demultiplexed in R (version 4.1.1). The *dada2* package was used to denoise the sequences, filter and trim reads, dereplicate reads, merge paired end reads, generate an amplicon sequence variant table, remove chimeras and generate a Phyloseq object. The Silva database (version 138.1) was used to assign taxonomy. Mitochondria and chloroplasts were filtered out of the dataset using the Phyloseq package (version 1.46.0). Phyloseq was used for downstream analysis of relative abundance and taxa richness. The DESeq2 package (version 1.42.0) was used to measure differential abundance. The ggplot2 package (version 3.5.0) was used to generate heatmap and relative abundance plots. The vegan package (version 2.6-4) was used to measure Bray Curtis distance.

Diet formulations

These diets were custom-formulated at University of Alabama at Birmingham.

	Z17-D01	**Z17-D02**
	High Protein	**Low Protein**
Ingredient	**%**	**%**
casein - low trace metals	30.00	15.00
fish protein hydrolysate	27.00	13.50
alpha cellulose	8.00	8.00
wheat starch	5.09	23.00
dextrin	4.00	4.00
safflower oil	4.00	5.00
soy lecithin (refined)	4.00	4.00
vitamin mix (MP-VDFM)	4.00	4.00
diatomaceous earth	3.20	12.29
alginate (TIC algin 400)	3.00	3.00
mineral mix (BTm)	3.00	3.00
menhaden fish oil (ARBP)	2.00	2.50
potassium phosphate monobasic	1.15	1.15
canthaxanthin (10%)	1.00	1.00
glucosamine	0.25	0.25
betaine	0.15	0.15
cholesterol	0.12	0.12
ascorbylpalmitate	0.04	0.04
Total	100.00	100.00
Calculated Protein (%)	50.10	25.05

Calculated Fat (%)	13.12	13.12
Calculated Carbohydrate (%)	12.41	30.32
Calculated Energy (cal/g)	4567	3868

References:

Ahuja, Malini, Daniella M. Schwartz, Mayank Tandon, Aran Son, Mei Zeng, William Swaim, Michael Eckhaus, et al. 2017. "Orai1-Mediated Antimicrobial Secretion from Pancreatic Acini Shapes the Gut Microbiome and Regulates Gut Innate Immunity." *Cell Metabolism* 25 (3): 635–46. https://doi.org/10.1016/j.cmet.2017.02.007.

Alvers, Ashley L., Sean Ryan, Paul J. Scherz, Jan Huisken, and Michel Bagnat. 2014. "Single Continuous Lumen Formation in the Zebrafish Gut Is Mediated by Smoothened-Dependent Tissue Remodeling." *Development (Cambridge)* 141 (5): 1110–19. https://doi.org/10.1242/dev.100313.

Bao, Honghong, Yi Wang, Hanlin Xiong, Yaoyao Xia, Zhifu Cui, and Lingbin Liu. 2024. "Mechanism of Iron Ion Homeostasis in Intestinal Immunity and Gut Microbiota Remodeling." *International Journal of Molecular Sciences*. Multidisciplinary Digital Publishing Institute (MDPI). https://doi.org/10.3390/ijms25020727.

Belkaid, Yasmine, and Timothy W Hand. 2014. "Role of the Microbiota in Immunity and Inflammation." *Cell* 157: 121–41. https://doi.org/10.1016/j.cell.2014.03.011.

Bessede, Alban, Marco Gargaro, Maria T. Pallotta, Davide Matino, Giuseppe Servillo, Cinzia Brunacci, Silvio Bicciato, et al. 2014. "Aryl Hydrocarbon Receptor Control of a Disease Tolerance Defence Pathway." *Nature* 511 (7508): 184–90. https://doi.org/10.1038/nature13323.

Birchenough, G. M.H., M. E.V. Johansson, J. K. Gustafsson, J. H. Bergström, and G. C. Hansson. 2015. "New Developments in Goblet Cell Mucus Secretion and Function." *Mucosal Immunology* 8 (4): 712–19. https://doi.org/10.1038/mi.2015.32.

Bohórquez, Diego V, Rafiq A Shahid, Alan Erdmann, Alex M Kreger, Yu Wang, Nicole Calakos, Fan Wang, and Rodger A Liddle. 2015. "Neuroepithelial Circuit Formed by Innervation of Sensory Enteroendocrine Cells." *Journal of Clinical Investigation* 125 (2): 782–86. https://doi.org/10.1172/JCI78361DS1.

Camp, J. Gray, Christopher L. Frank, Colin R. Lickwar, Harendra Guturu, Tomas Rube, Aaron M. Wenger, Jenny Chen, Gill Bejerano, Gregory E. Crawford, and John F. Rawls. 2014. "Microbiota Modulate Transcription in the Intestinal Epithelium without Remodeling the Accessible Chromatin Landscape." *Genome Research* 24 (9): 1504–16. https://doi.org/10.1101/gr.165845.113.

Camp, J. Gray, Amelia L. Jazwa, Chad M. Trent, and John F. Rawls. 2012. "Intronic Cis-Regulatory Modules Mediate Tissue-Specific and Microbial Control of Angptl4/Fiaf Transcription." *PLoS Genetics* 8 (3). https://doi.org/10.1371/journal.pgen.1002585.

Choi, Harry M.T., Maayan Schwarzkopf, Mark E. Fornace, Aneesh Acharya, Georgios Artavanis, Johannes Stegmaier, Alexandre Cunha, and Niles A. Pierce. 2018. "Third-Generation in Situ Hybridization Chain Reaction: Multiplexed, Quantitative, Sensitive, Versatile, Robust." *Development (Cambridge)* 145 (12): 1–10. https://doi.org/10.1242/dev.165753.

Cholan, Pradeep Manuneedhi, Alvin Han, Brad R. Woodie, Maxinne Watchon, Angela R.M. Kurz, Angela S. Laird, Warwick J. Britton, et al. 2020. "Conserved Anti-Inflammatory Effects and Sensing of Butyrate in Zebrafish." *Gut Microbes* 12 (1): 1–11. https://doi.org/10.1080/19490976.2020.1824563.

Cocchiaro, Jordan;, and John F Rawls. 2013. "Microgavage of Zebrafish Larvae." *JoVE*, no. 72: e4434. https://doi.org/doi:10.3791/4434.

Dostal, Alexandra, Christophe Chassard, Florentine M. Hilty, Michael B. Zimmermann, Tanja Jaeggi, Samuela Rossi, and Christophe Lacroix. 2012. "Iron Depletion and Repletion with Ferrous Sulfate or Electrolytic Iron Modifies the Composition and Metabolic Activity of the Gut Microbiota in Rats." *Journal of Nutrition* 142 (2): 271–77. https://doi.org/10.3945/jn.111.148643.

Dubytska, Lidiya P., Ranjan Koirala, Azhia Sanchez, and Ronald Thune. 2022. "Edwardsiella Ictaluri T3SS Effector EseN Modulates Expression of Host Genes Involved in the Immune Response." *Microorganisms* 10 (7): 1–15. https://doi.org/10.3390/microorganisms10071334.

Dunn, Louise L., Yohan Suryo Rahmanto, and Des R. Richardson. 2007. "Iron Uptake and Metabolism in the New Millennium." *Trends in Cell Biology*. https://doi.org/10.1016/j.tcb.2006.12.003.

Franzenburg, Sören, Sebastian Fraune, Sven Künzel, John F. Baines, Tomislav Domazet-Lošo, and Thomas C.G. Bosch. 2012. “MyD88-Deficient Hydra Reveal an Ancient Function of TLR Signaling in Sensing Bacterial Colonizers.” *Proceedings of the National Academy of Sciences of the United States of America* 109 (47): 19374–79. https://doi.org/10.1073/pnas.1213110109.

Gibson, D. L., C. Ma, K. S.B. Bergstrom, J. T. Huang, C. Man, and B. A. Vallance. 2008. “MyD88 Signalling Plays a Critical Role in Host Defence by Controlling Pathogen Burden and Promoting Epithelial Cell Homeostasis during Citrobacterrodentium-Induced Colitis.” *Cellular Microbiology* 10 (3): 618–31. https://doi.org/10.1111/j.1462-5822.2007.01071.x.

Goldspink, Deborah A, Frank Reimann, and Fiona M Gribble. 2018. “Models and Tools for Studying Enteroendocrine Cells.” *Endocrinology* 159 (12): 3874–84. https://doi.org/10.1210/en.2018-00672.

Gonnella, P. A., and M. R. Neutra. 1984. “Membrane-Bound and Fluid-Phase Macromolecules Enter Separate Prelysosomal Compartments in Absorptive Cells of Suckling Rat Ileum.” *Journal of Cell Biology* 99 (3): 909–17. https://doi.org/10.1083/jcb.99.3.909.

Graney, Daniel O. 1968. “The Uptake of Ferritin by Ileal Absorptive Cells in Suckling Rats. an Electron Microscope Study.” *American Journal of Anatomy* 123 (2): 227–53. https://doi.org/10.1002/aja.1001230202.

Graustein, Andrew D., Elizabeth A. Misch, Munyaradzi Musvosvi, Muki Shey, Javeed A. Shah, Chetan Seshadri, Augustine Aguoju, et al. 2018. “Toll-like Receptor Chaperone HSP90B1 and the Immune Response to Mycobacteria.” *PLoS ONE* 13 (12): 1–18. https://doi.org/10.1371/journal.pone.0208940.

Harper, James, Arne Mould, Robert M. Andrews, Elizabeth K. Bikoff, and Elizabeth J. Robertson. 2011. “The Transcriptional Repressor Blimp1/Prdm1 Regulates Postnatal Reprogramming of Intestinal Enterocytes.” *Proceedings of the National Academy of Sciences of the United States of America* 108 (26): 10585–90. https://doi.org/10.1073/pnas.1105852108.

Jones, Lena O, Reegan J Willms, Minjeong Shin, Xinyue Xu, Mckenna Eklund, Ralph Derrick V Graham, and Edan Foley. 2023. “Single Cell Resolution of the Adult Zebrafish Intestine Under Conventional Conditions, and in Response To an Acute Vibrio Cholerae Infection.” *Cell Reports* 42 (11): 2023.04.14.536919. https://doi.org/10.1016/j.celrep.2023.113407.

Kanther, Michelle, Xiaolun Sun, Marcus Mhlbauer, Lantz C. MacKey, Edward J. Flynn, Michel Bagnat, Christian Jobin, and John F. Rawls. 2011. “Microbial Colonization Induces Dynamic Temporal and Spatial Patterns of NF-KB Activation in the Zebrafish Digestive Tract.” *Gastroenterology* 141 (1): 197–207. https://doi.org/10.1053/j.gastro.2011.03.042.

Karmarkar, Dipti, and Kenneth L. Rock. 2013. “Microbiota Signalling through MyD88 Is Necessary for a Systemic Neutrophilic Inflammatory Response.” *Immunology* 140 (4): 483–92. https://doi.org/10.1111/imm.12159.

Kau, Andrew L., Philip P. Ahern, Nicholas W. Griffin, Andrew L. Goodman, and Jeffrey I. Gordon. 2011. “Human Nutrition, the Gut Microbiome and the Immune System.” *Nature* 474 (7351): 327–36. https://doi.org/10.1038/nature10213.

Keebaugh, Erin S., Ryuichi Yamada, Benjamin Obadia, William B. Ludington, and William W. Ja. 2018. “Microbial Quantity Impacts Drosophila Nutrition, Development, and Lifespan.” *IScience* 4: 247–59. https://doi.org/10.1016/j.isci.2018.06.004.

Kim, Boram, Makoto I Kanai, Yangkyun Oh, Minsoo Kyung, Eun-kyoung Kim, In-hwan Jang, Ji-hoon Lee, Sang-gyu Kim, Greg S B Suh, and Won-jae Lee. 2021. “Response of the Microbiome – Gut – Brain Axis in Drosophila to Amino Acid Deficit.” *Nature*, no. March 2020. https://doi.org/10.1038/s41586-021-03522-2.

Koyanagi, Takashi, Akira Nakagawa, Haruko Sakurama, Keiko Yamamoto, Naofumi Sakurai, Yukinobu Takagi, Hiromichi Minami, Takane Katayama, and Hidehiko Kumagai. 2012. “Eukaryotic-Type Aromatic Amino Acid Decarboxylase from the Root Colonizer Pseudomonas Putida Is Highly Specific for 3,4-Dihydroxyphenyl-l-Alanine, an Allelochemical in the Rhizosphere.” *Microbiology (United Kingdom)* 158 (12): 2965–74. https://doi.org/10.1099/mic.0.062463-0.

Kraehenbuhl, J. P., and M. A. Campiche. 1969. “Early Stages of Intestinal Absorption of Specific Antibiodies in the Newborn. An Ultrastructural, Cytochemical, and Immunological Study in the Pig, Rat, and Rabbit.” *The Journal of Cell Biology* 42 (2): 345–65. https://doi.org/10.1083/jcb.42.2.345.

Lesperance, Danielle N.A., and Nichole A. Broderick. 2020. “Gut Bacteria Mediate Nutrient Availability in Drosophila Diets.” *Applied and Environmental Microbiology* 87 (1): 1–14. https://doi.org/10.1128/AEM.01401-20.

Li, Pingping, Jinhua Zhang, Xiaoyi Liu, Lu Gan, Yi Xie, Hong Zhang, and Jing Si. 2022. “The Function and the Affecting Factors of the Zebrafish Gut Microbiota.” *Frontiers in Microbiology* 13 (June). https://doi.org/10.3389/fmicb.2022.903471.

Lickwar, Colin R., J. Gray Camp, Matthew Weiser, Jordan L. Cocchiaro, David M. Kingsley, Terrence S. Furey, Shehzad Z. Sheikh, and John F. Rawls. 2017. *Genomic Dissection of Conserved Transcriptional Regulation in Intestinal Epithelial Cells*. *PLoS Biology*. Vol. 15. https://doi.org/10.1371/journal.pbio.2002054.

Logan, Savannah L., Jacob Thomas, Jinyuan Yan, Ryan P. Baker, Drew S. Shields, Joao B. Xavier, Brian K. Hammer, and Raghuveer Parthasarathy. 2018. “The Vibrio Cholerae Type VI Secretion System Can Modulate Host Intestinal Mechanics to Displace Gut Bacterial Symbionts.” *Proceedings of the National Academy of Sciences of the United States of America* 115 (16): E3779–87. https://doi.org/10.1073/pnas.1720133115.

Long, Jonathan Z., Katrin J. Svensson, Leslie A. Bateman, Hua Lin, Theodore Kamenecka, Isha A. Lokurkar, Jesse Lou, et al. 2016. “The Secreted Enzyme PM20D1 Regulates Lipidated Amino Acid Uncouplers of Mitochondria.” *Cell* 166 (2): 424–35. https://doi.org/10.1016/j.cell.2016.05.071.

Lu, Yanhui, Haidong Zhu, Xiaoling Wang, Harold Snieder, Ying Huang, Gregory A. Harshfield, Frank A. Treiber, and Yanbin Dong. 2006. “Effects of Dopamine Receptor Type 1 and Gs Protein α Subunit Gene Polymorphisms on Blood Pressure at Rest and in Response to Stress.” *American Journal of Hypertension* 19 (8): 832–36. https://doi.org/10.1016/j.amjhyper.2006.01.006.

Mahoney, James A., Bongi Ntolosi, Rosangela P. DaSilva, Siamon Gordon, and Andrew J. McKnight. 2001. “Cloning and Characterization of CPVL, a Novel Serine Carboxypeptidase, from Human Macrophages.” *Genomics* 72 (3): 243–51. https://doi.org/10.1006/geno.2000.6484.

Martinez-Guryn, Kristina, Nathaniel Hubert, Katya Frazier, Saskia Urlass, Mark W. Musch, Patricia Ojeda, Joseph F. Pierre, et al. 2018. “Small Intestine Microbiota Regulate Host Digestive and Absorptive Adaptive Responses to Dietary Lipids.” *Cell Host and Microbe* 23 (4): 458-469.e5. https://doi.org/10.1016/j.chom.2018.03.011.

Marwaha, Rituraj, and Mahak Sharma. 2017. “DQ-Red BSA Trafficking Assay in Cultured Cells to Assess Cargo Delivery to Lysosomes.” *Bio-Protocol* 7 (19). https://doi.org/10.21769/bioprotoc.2571.

Massaquoi, Michelle S., Garth L. Kong, Daisy Chilin-Fuentes, Julia S. Ngo, Patrick F. Horve, Ellie Melancon, M. Kristina Hamilton, Judith S. Eisen, and Karen Guillemin. 2023. “Cell-Type-Specific Responses to the Microbiota across All Tissues of the Larval Zebrafish.” *Cell Reports* 42 (2): 112095. https://doi.org/10.1016/j.celrep.2023.112095.

Mayneris-Perxachs, Jordi, José María Moreno-Navarrete, and José Manuel Fernández-Real. 2022. “The Role of Iron in Host–Microbiota Crosstalk and Its Effects on Systemic Glucose Metabolism.” *Nature Reviews Endocrinology* 18 (11): 683–98. https://doi.org/10.1038/s41574-022-00721-3.

Mcdermott, Andrew J., and Gary B. Huffnagle. 2014. “The Microbiome and Regulation of Mucosal Immunity.” *Immunology* 142 (1): 24–31. https://doi.org/10.1111/imm.12231.

Meixner, Arabella, Florian Karreth, Lukas Kenner, and Erwin F. Wagner. 2004. “JunD Regulates Lymphocyte Proliferation and T Helper Cell Cytokine Expression.” *EMBO Journal* 23 (6): 1325–35. https://doi.org/10.1038/sj.emboj.7600133.

Munjal, Akankshi, Edouard Hannezo, Tony Y.C. Tsai, Timothy J. Mitchison, and Sean G. Megason. 2021. “Extracellular Hyaluronate Pressure Shaped by Cellular Tethers Drives Tissue Morphogenesis.” *Cell* 184 (26): 6313-6325.e18. https://doi.org/10.1016/j.cell.2021.11.025.

Murdoch, Caitlin C., Scott T. Espenschied, Molly A. Matty, Olaf Mueller, David M. Tobin, and John F. Rawls. 2019. “Intestinal Serum Amyloid a Suppresses Systemic Neutrophil Activation and Bactericidal Activity in Response to Microbiota Colonization.” *PLoS Pathogens* 15 (3). https://doi.org/10.1371/journal.ppat.1007381.

Nakayama, Satoshi, Toshio Sekiguchi, and Michio Ogasawara. 2019. “Molecular and Evolutionary Aspects of the Protochordate Digestive System,” 309–20.

Ngo, Julia S, Piyush Amitabh, Jonah G Sokoloff, Calvin Trinh, Travis J Wiles, Karen Guillemin, and Raghuveer Parthasarathy. 2024. “Bacterial Modulation of Intestinal Motility through Macrophage Redistribution.”

———. 2024. “The Vibrio Type VI Secretion System Induces Intestinal Macrophage Redistribution and Enhanced Intestinal Motility.” *MBio*.

Noaillac-Depeyre, J, and N Gas. 1976. “Electron Microscopic Study on Gut Epithelium of the Tench (Tinca Tinca L.) with Respect to Its Absorptive Functions.” *Tissue & Cell* 8 (3): 511–30.

https://doi.org/10.1016/0040-8166(76)90010-0.
Park, Jieun, Daniel S. Levic, Kaelyn D. Sumigray, Jennifer Bagwell, Oznur Eroglu, Carina L. Block, Cagla Eroglu, et al. 2019. “Lysosome-Rich Enterocytes Mediate Protein Absorption in the Vertebrate Gut.” *Developmental Cell* 51 (1): 7-20.e6. https://doi.org/10.1016/j.devcel.2019.08.001.
Pham, Linh N., Michelle Kanther, Ivana Semova, and John F. Rawls. 2008. “Methods for Generating and Colonizing Gnotobiotic Zebrafish.” *Nature Protocols* 3 (12): 1862–75. https://doi.org/10.1038/nprot.2008.186.
Rodríguez-Fraticelli, Alejo E., Jennifer Bagwell, Minerva Bosch-Fortea, Gaelle Boncompain, Natalia Reglero-Real, Maria J. García-León, Germán Andrés, et al. 2015. “Developmental Regulation of Apical Endocytosis Controls Epithelial Patterning in Vertebrate Tubular Organs.” *Nature Cell Biology* 17 (3): 241–50. https://doi.org/10.1038/ncb3106.
Roeselers, Guus, Erika K. Mittge, W. Zac Stephens, David M. Parichy, Colleen M. Cavanaugh, Karen Guillemin, and John F. Rawls. 2011. “Evidence for a Core Gut Microbiota in the Zebrafish.” *ISME Journal* 5 (10): 1595–1608. https://doi.org/10.1038/ismej.2011.38.
Rolig, Annah S., Raghuveer Parthasarathy, Adam R. Burns, Brendan J.M. Bohannan, and Karen Guillemin. 2015. “Individual Members of the Microbiota Disproportionately Modulate Host Innate Immune Responses.” *Cell Host and Microbe* 18 (5): 613–20. https://doi.org/10.1016/j.chom.2015.10.009.
Rombout, J H, C H Lamers, M H Helfrich, A Dekker, and J J Taverne-Thiele. 1985. “Uptake and Transport of Intact Macromolecules in the Intestinal Epithelium of Carp (Cyprinus Carpio L.) and the Possible Immunological Implications.” *Cell and Tissue Research* 239 (3): 519–30. https://doi.org/10.1007/BF00219230.
Sar, Astrid M van der, Oliver W Stockhammer, Carina van der Laan, Herman P Spaink, Wilbert Bitter, and Annemarie H Meijer. 2006. “MyD88 Innate Immune Function in a Zebrafish Embryo Infection Model.” *Infection and Immunity* 74 (4): 2436–41. https://doi.org/10.1128/IAI.74.4.2436-2441.2006.
Satija, Rahul, Jeffrey A. Farrell, David Gennert, Alexander F. Schier, and Aviv Regev. 2015. “Spatial Reconstruction of Single-Cell Gene Expression Data.” *Nature Biotechnology* 33 (5): 495–502. https://doi.org/10.1038/nbt.3192.
Sekyere, Eric O., Louise L. Dunn, Yohan Suryo Rahmanto, and Des R. Richardson. 2006. “Role of Melanotransferrin in Iron Metabolism: Studies Using Targeted Gene Disruption in Vivo.” *Blood* 107 (7): 2599–2601. https://doi.org/10.1182/blood-2005-10-4174.
Semova, Ivana, Juliana D. Carten, Jesse Stombaugh, Lantz C. MacKey, Rob Knight, Steven A. Farber, and John F. Rawls. 2012. “Microbiota Regulate Intestinal Absorption and Metabolism of Fatty Acids in the Zebrafish.” *Cell Host and Microbe* 12 (3): 277–88. https://doi.org/10.1016/j.chom.2012.08.003.
Shaner, Nathan C., Robert E. Campbell, Paul A. Steinbach, Ben N.G. Giepmans, Amy E. Palmer, and Roger Y. Tsien. 2004. “Improved Monomeric Red, Orange and Yellow Fluorescent Proteins Derived from Discosoma Sp. Red Fluorescent Protein.” *Nature Biotechnology* 22 (12): 1567–72. https://doi.org/10.1038/nbt1037.
Smith, Michelle I., Tanya Yatsunenko, Mark J. Manary, Indi Trehan, Rajhab Mkakosya, Jiye Cheng, Andrew L. Kau, et al. 2013. “Gut Microbiomes of Malawian Twin Pairs Discordant for Kwashiorkor.” *Science* 339 (6119): 548–54. https://doi.org/10.1126/science.1229000.
Sommer, Christoph, Christoph Straehle, Ullrich Kothe, and Fred A. Hamprecht. 2011. “Ilastik: Interactive Learning and Segmentation Toolkit.” *Proceedings - International Symposium on Biomedical Imaging*, 230–33. https://doi.org/10.1109/ISBI.2011.5872394.
Stephens, W. Zac, Adam R. Burns, Keaton Stagaman, Sandi Wong, John F. Rawls, Karen Guillemin, and Brendan J.M. Bohannan. 2016. “The Composition of the Zebrafish Intestinal Microbial Community Varies across Development.” *ISME Journal* 10 (3): 644–54. https://doi.org/10.1038/ismej.2015.140.
Stroband, H W, and F M Debets. 1978. “The Ultrastructure and Renewal of the Intestinal Epithelium of the Juvenile Grasscarp, Ctenopharyngodon Idella (Val.).” *Cell and Tissue Research* 187 (2): 181–200. https://doi.org/10.1007/BF00224364.
Sur, Abhinav, Yiqun Wang, Paulina Capar, Gennady Margolin, Morgan Kathleen Prochaska, and Jeffrey A. Farrell. 2023. “Single-Cell Analysis of Shared Signatures and Transcriptional Diversity during Zebrafish Development.” *Developmental Cell* 58 (24): 3028-3047.e12. https://doi.org/10.1016/j.devcel.2023.11.001.
Swanson, J A, B D Yirinec, and S C Silverstein. 1985. “Phorbol Esters and Horseradish Peroxidase Stimulate Pinocytosis and Redirect the Flow of Pinocytosed Fluid in Macrophages.” *The Journal of*

Cell Biology 100 (3): 851–59. https://doi.org/10.1083/jcb.100.3.851.
Tingaud-Sequeira, Angèle, and Joan Cerdà. 2007. “Phylogenetic Relationships and Gene Expression Pattern of Three Different Cathepsin L (Ctsl) Isoforms in Zebrafish: Ctsla Is the Putative Yolk Processing Enzyme.” *Gene* 386 (1–2): 98–106. https://doi.org/10.1016/j.gene.2006.08.018.
Vaart, Michiel Van Der, Joost J. Van Soest, Herman P. Spaink, and Annemarie H. Meijer. 2013. “Functional Analysis of a Zebrafish Myd88 Mutant Identifies Key Transcriptional Components of the Innate Immune System.” *DMM Disease Models and Mechanisms* 6 (3): 841–54. https://doi.org/10.1242/dmm.010843.
Vortherms, Timothy A., Chau H. Nguyen, Murat Bastepe, Harald Jüppner, and Val J. Watts. 2006. “D2 Dopamine Receptor-Induced Sensitization of Adenylyl Cyclase Type 1 Is Gαs Independent.” *Neuropharmacology* 50 (5): 576–84. https://doi.org/10.1016/j.neuropharm.2005.11.004.
Wallace, Kenneth N., Shafinaz Akhter, Erin M. Smith, Kristin Lorent, and Michael Pack. 2005. “Intestinal Growth and Differentiation in Zebrafish.” *Mechanisms of Development* 122 (2): 157–73. https://doi.org/10.1016/j.mod.2004.10.009.
Wang, Kuan Wen, Xiaoming Zhan, William McAlpine, Zhao Zhang, Jin Huk Choi, Hexin Shi, Takuma Misawa, et al. 2019. “Enhanced Susceptibility to Chemically Induced Colitis Caused by Excessive Endosomal TLR Signaling in LRBA-Deficient Mice.” *Proceedings of the National Academy of Sciences of the United States of America* 166 (23): 11380–89. https://doi.org/10.1073/pnas.1901407116.
Wen, Jia, Gilberto Padilla Mercado, Alyssa Volland, Heidi L. Doden, Colin R. Lickwar, Taylor Crooks, Genta Kakiyama, et al. 2021. “Fxr Signaling and Microbial Metabolism of Bile Salts in the Zebrafish Intestine.” *Science Advances* 7 (30): 1–20. https://doi.org/10.1126/sciadv.abg1371.
Westerfield, M. 2000. *The Zebrafish Book. A Guide for the Laboratory Use of Zebrafish (Danio Rerio)*. Fourth. University of Oregon Press.
Wiles, Travis J., Brandon H. Schlomann, Elena S. Wall, Reina Betancourt, Raghuveer Parthasarathy, and Karen Guillemin. 2020. *Swimming Motility of a Gut Bacterial Symbiont Promotes Resistance to Intestinal Expulsion and Enhances Inflammation*. *PLoS Biology*. Vol. 18. https://doi.org/10.1371/journal.pbio.3000661.
Willms, Reegan J., Lena O. Jones, Jennifer C. Hocking, and Edan Foley. 2022. “A Cell Atlas of Microbe-Responsive Processes in the Zebrafish Intestine.” *Cell Reports* 38 (5). https://doi.org/10.1016/j.celrep.2022.110311.
Wilson, Annette S., Kathryn R. Koller, Matsepo C. Ramaboli, Lucky T. Nesengani, Soeren Ocvirk, Caixia Chen, Christie A. Flanagan, et al. 2020. “Diet and the Human Gut Microbiome: An International Review.” *Digestive Diseases and Sciences*. Springer. https://doi.org/10.1007/s10620-020-06112-w.
Wilson, J. M., J. A. Whitney, and M. R. Neutra. 1987. “Identification of an Endosomal Antigen Specific to Absorptive Cells of Suckling Rat Ileum.” *Journal of Cell Biology* 105 (2): 691–703. https://doi.org/10.1083/jcb.105.2.691.
Worthington, J. J., F. Reimann, and F. M. Gribble. 2018. “Enteroendocrine Cells-Sensory Sentinels of the Intestinal Environment and Orchestrators of Mucosal Immunity.” *Mucosal Immunology* 11 (1): 3–20. https://doi.org/10.1038/mi.2017.73.
Xue, Chen, Ganglei Li, Qiuxian Zheng, Xinyu Gu, Qingmiao Shi, Yuanshuai Su, Qingfei Chu, et al. 2023. “Tryptophan Metabolism in Health and Disease.” *Cell Metabolism*. Cell Press. https://doi.org/10.1016/j.cmet.2023.06.004.
Yamada, Ryuichi, Sonali A. Deshpande, Kimberley D. Bruce, Elizabeth M. Mak, and William W. Ja. 2015. “Microbes Promote Amino Acid Harvest to Rescue Undernutrition in Drosophila.” *Cell Reports* 10 (6): 865–72. https://doi.org/10.1016/j.celrep.2015.01.018.
Ye, Lihua, Olaf Mueller, Jennifer Bagwell, Michel Bagnat, Rodger A. Liddle, and John F. Rawls. 2019. “High Fat Diet Induces Microbiota-Dependent Silencing of Enteroendocrine Cells.” *ELife*. https://doi.org/10.1101/658435.
Yee, Nelson S., Kristin Lorent, and Michael Pack. 2005. “Exocrine Pancreas Development in Zebrafish.” *Developmental Biology* 284 (1): 84–101. https://doi.org/10.1016/j.ydbio.2005.04.035.
Yilmaz, Bahtiyar, and Hai Li. 2018. “Gut Microbiota and Iron: The Crucial Actors in Health and Disease.” *Pharmaceuticals*. MDPI AG. https://doi.org/10.3390/ph11040098.
Yonge, C.M. 1923. “The Mechanism of Feeding, Digestion, and Assimilation in the Lamellibranch Mya.” *Studies on the Comparative Physiology of Digestion*, 15–63. https://doi.org/10.1093/geronj/19.1.83.
Zaneveld, Jesse R., Ryan McMinds, and Rebecca Vega Thurber. 2017. “Stress and Stability: Applying

the Anna Karenina Principle to Animal Microbiomes." *Nature Microbiology* 2 (August). https://doi.org/10.1038/nmicrobiol.2017.121.

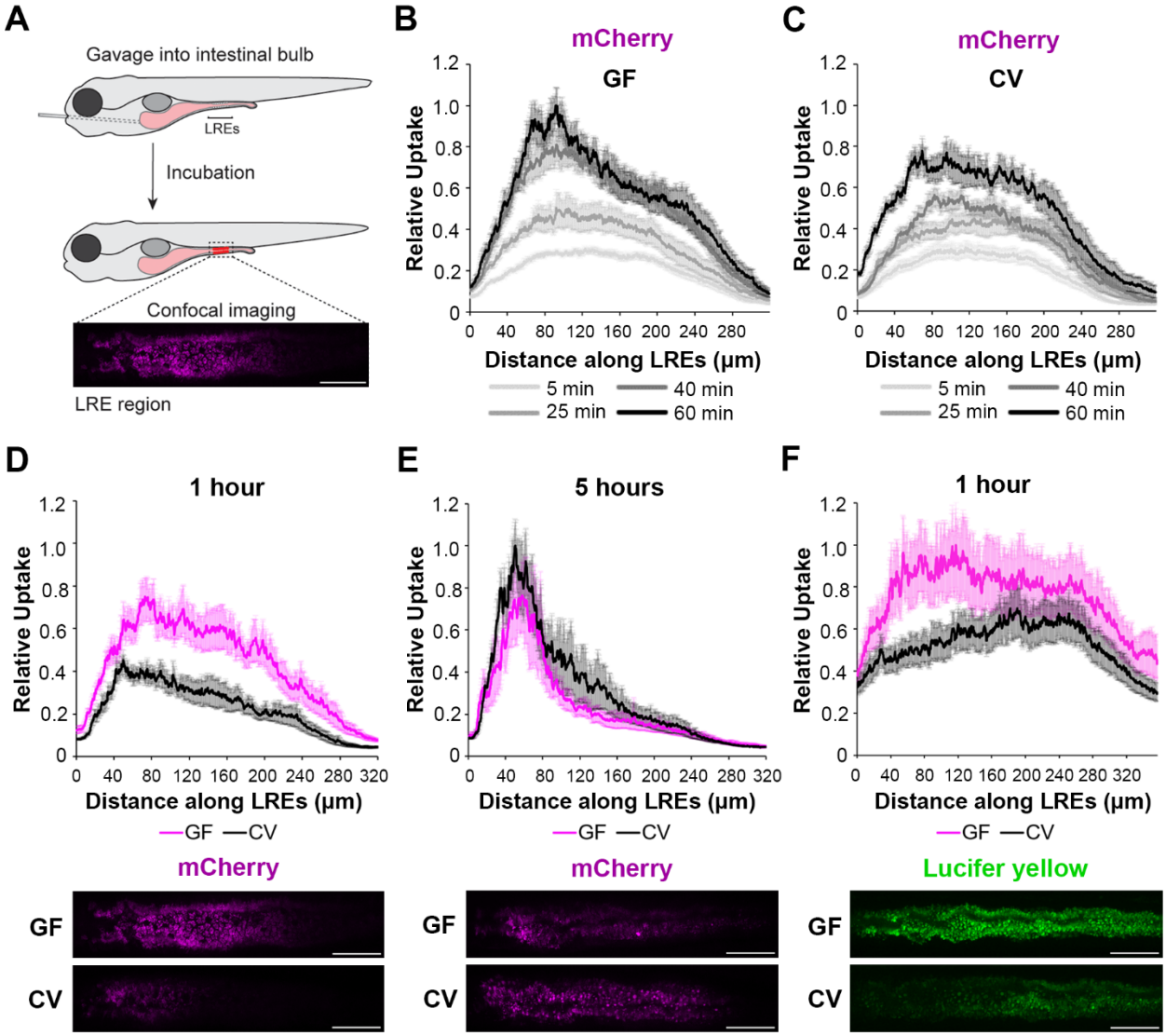

Figure 1. Microbes slow the rate of soluble cargo uptake in LREs.

(A) Cartoon depicting experimental design of the gavage assay in GF and CV larvae. Following derivation under conventional (CV) or germ-free (GF) conditions, 6 dpf larvae were gavaged, and uptake of luminal cargoes by LREs was measured by confocal microscopy in the LRE region (approximately 300 μm in length).

(B, C) Plots of normalized mCherry fluorescence intensity along the LRE region over time in 6 dpf GF (B) and CV (C) larvae. Minutes after gavage, LREs rapidly took up and quickly accumulate mCherry in GF larvae. The anterior LREs approached full saturation by 40 minutes post gavage. Cargo uptake was slower in CV larvae, and anterior LREs did not reach saturation by 40 minutes post gavage.

(D, E) Top: Plots of normalized mCherry fluorescence intensity along the LRE region of GF and CV larvae at 1 (D) and 5 (E) hours PG. GF larvae internalized significantly more mCherry than CV larvae (2-way ANOVA, $p < 0.0001$, $n = 8 - 10$) one hour PG, and CV larvae reached a similar level of mCherry accumulation to GF larvae by 5 hours PG (2-way ANOVA, $p = 0.137$, $n = 8 - 11$). Bottom: Representative confocal images showing mCherry signal in the LRE region (scale bars = 50 μm).

(F) Top: Plot of normalized lucifer yellow fluorescence intensity along the LRE region of GF and CV larvae at 1 hour post gavage. LREs in GF larvae internalized significantly more Lucifer yellow than CV larvae by 1 hour post gavage (2-way ANOVA, $p < 0.0001$, $n = 8$).

1107
1108

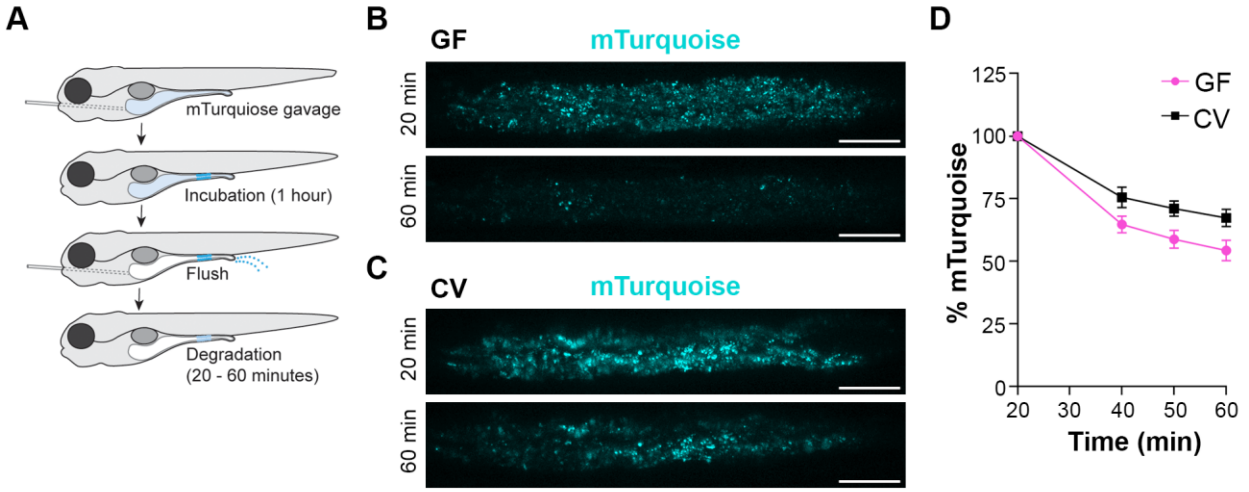

1109
1110 **Figure 2. LRE protein degradation activity is reduced by microbes.**
1111 (A) Cartoon depicting the experimental design of pulse-chase protein uptake and degradation assay. At 6 dpf, GF and
1112 CV larvae were gavaged with mTurquoise (25 mg/mL), incubated for 1 hour, and then flushed with PBS to remove
1113 luminal mTurquoise. LRE degradation of mTurquoise was measured by confocal microscopy over time.
1114 (B, C) Confocal images of mTurquoise fluorescence in the LRE region after flushing in GF (B) and CV (C) larvae (scale
1115 bars = 50 μm).
1116 (D) Plot showing the degradation of mTurquoise fluorescence (%) in the LRE region over time. Degradation occurred
1117 at a significantly faster rate in GF than CV larvae from 20 – 60 minutes post gavage (Simple linear regression, p =
1118 0.0167, n = 6).

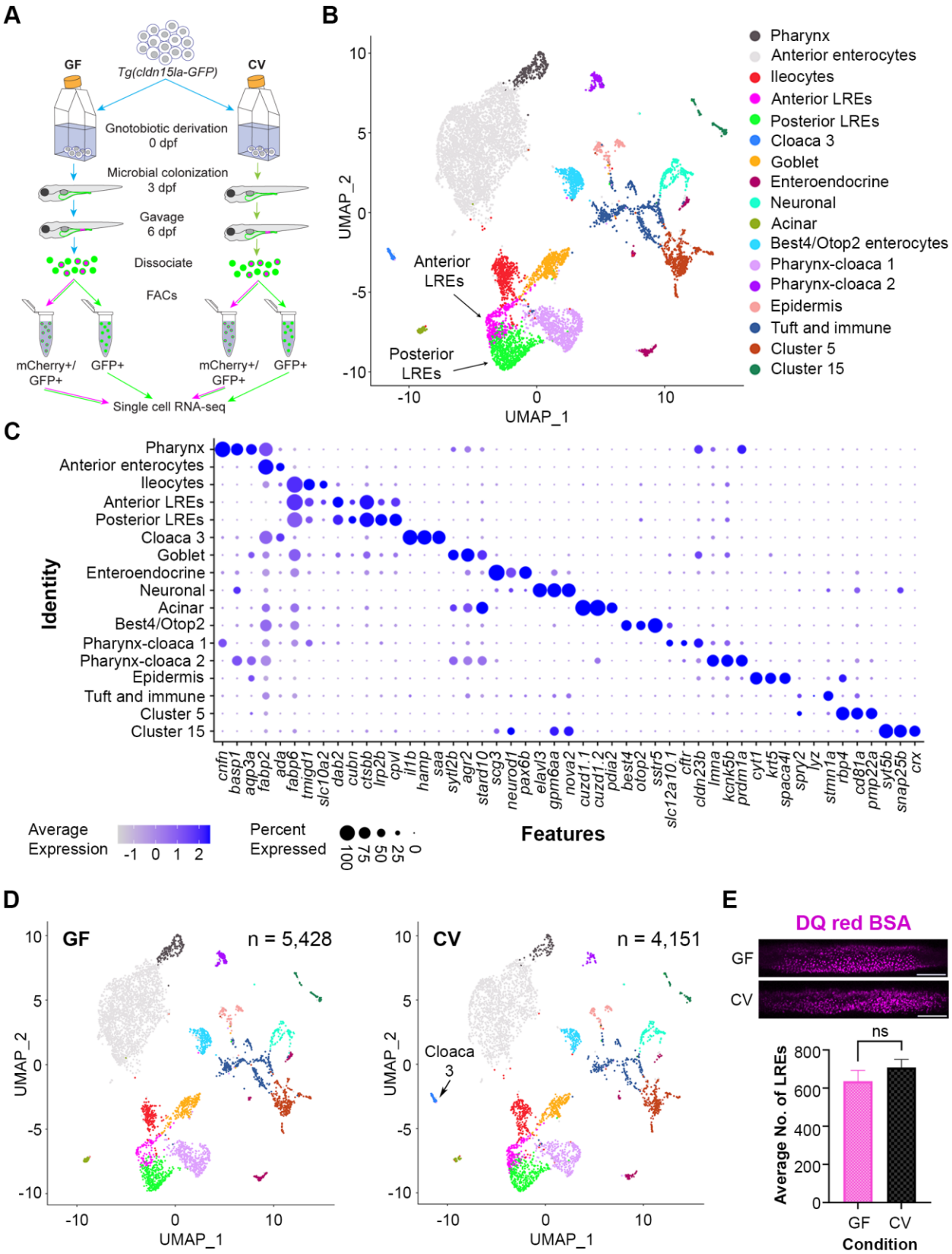

Figure 3. Single cell clustering reveals anterior and posterior LREs, microbially-responsive cloaca cells.

1122 (A) Cartoon depicting experimental design for transcriptomic profiling of intestinal cells in GF and CV larvae. GF and
1123 CV larvae expressing *Tg(cldn15la-GFP)* to label all intestinal epithelial cells (IECs) were raised to 6 dpf in gnotobiotic
1124 conditions and then gavaged with mCherry (1.25 mg/mL). Cells from dissociated larvae were FACs sorted to isolate
1125 GFP-positive/mCherry-positive from GFP-positive/mCherry-negative populations prior to single cell sequencing.
1126 (B) UMAP projection of cells color coded by cluster identity.
1127 (C) Dot plot of top cluster markers in each cluster. Average expression of the marker gene in each cell cluster is
1128 signified by the color gradient. Dot size indicates the percentage of cells in each cluster expressing the marker.
1129 (D) UMAP projection of cells color coded by cluster identity in the GF (left) and CV (right) datasets. The Cloaca 3
1130 cluster only appeared in the CV dataset.
1131 (E) Bar plot showing that the average number of LREs in the GF and CV larvae was not significantly different (2-tailed
1132 t-test, $p = 0.33$, $n = 10$). LREs were labeled by gavaging with DQ red BSA (50 µg/mL) in a separate experiment, then
1133 quantified. Images show DQ red BSA marking LRE lysosomal vacuoles (scale bar = 50 µm).
1134

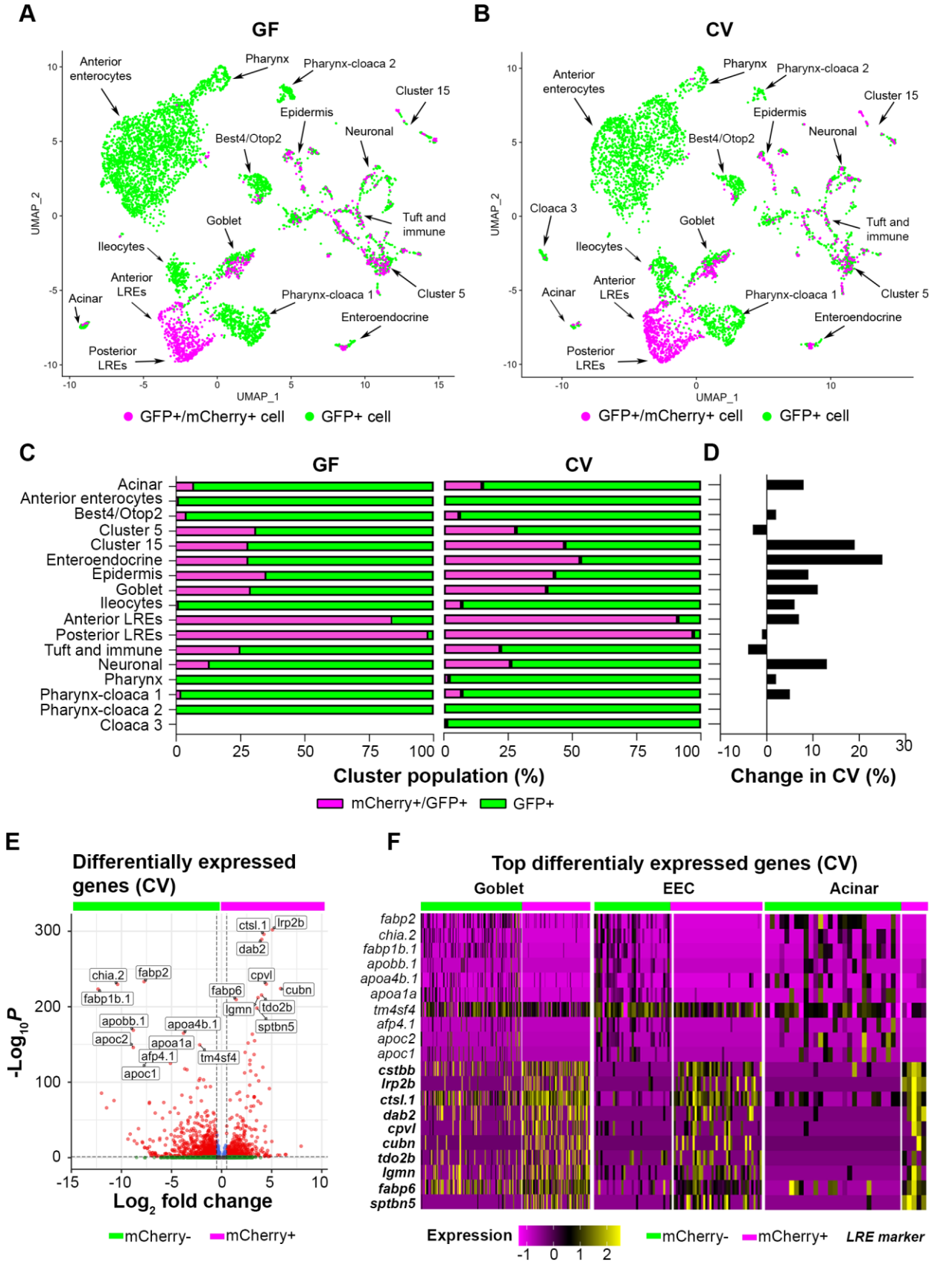
A
GF
Anterior enterocytes
Pharynx
Pharynx-cloaca 2
Cluster 15
Epidermis
Best4/Otop2
Neuronal
Goblet
Tuft and immune
Ileocytes
Anterior LREs
Acinar
Pharynx-cloaca 1
Cluster 5
Enteroendocrine
Posterior LREs
UMAP_1
UMAP_2
GFP+/mCherry+ cell
GFP+ cell
B
CV
Cloaca 3
C
D
Acinar
Anterior enterocytes
Best4/Otop2
Cluster 5
Cluster 15
Enteroendocrine
Epidermis
Goblet
Ileocytes
Anterior LREs
Posterior LREs
Tuft and immune
Neuronal
Pharynx
Pharynx-cloaca 1
Pharynx-cloaca 2
Cloaca 3
Cluster population (%)
Change in CV (%)
mCherry+/GFP+
GFP+
E
Differentially expressed genes (CV)
ctsl.1
lrp2b
dab2
chia.2
fabp2
cpvl
fabp6
cubn
fabp1b.1
lgmn
tdo2b
apobb.1
apoa4b.1
sptbn5
apoc2
apoa1a
afp4.1
tm4sf4
apoc1
-Log10P
Log2 fold change
mCherry-
mCherry+
F
Top differentialy expressed genes (CV)
Goblet
EEC
Acinar
fabp2
chia.2
fabp1b.1
apobb.1
apoa4b.1
apoa1a
tm4sf4
afp4.1
apoc2
apoc1
cstbb
lrp2b
ctsl.1
dab2
cpvl
cubn
tdo2b
lgmn
fabp6
sptbn5
Expression
mCherry-
mCherry+
LRE marker

1135
1136

1137 **Figure 4. Uptake of mCherry occurs in cells enriched in LRE markers.**
1138 (A, B) UMAP projections highlighting mCherry-positive/GFP-positive cells (magenta) and GFP-positive cells (green) in
1139 the GF and CV datasets.
1140 (C) Bar plots portray the percentage of mCherry-positive and mCherry-negative cells in the GF and CV datasets. Bar
1141 color indicates the proportion of mCherry-positive (magenta) and mCherry-negative (green) cells in each cluster.
1142 (D) Bar plot displays the difference in the proportion of mCherry-positive cells in the CV compared to the GF dataset.
1143 Positive values show that the proportion of mCherry-positive cells were higher in the CV dataset.
1144 (E) Volcano plot shows differentially expressed genes between mCherry-positive and mCherry-negative cells in the CV
1145 dataset. The x-axis displays the log fold change in expression between mCherry-positive and mCherry-negative cells,
1146 with positive values showing enhanced expression in mCherry-positive cells and negative values showing higher
1147 expression in mCherry-negative cells. Red points are genes with significantly different expression (padj < 0.05) and
1148 high fold change (log2FC < - 0.05, log2FC > 0.05).
1149 (F) Heatmap displays the expression of the top markers for mCherry-positive and mCherry-negative cells in goblet,
1150 EEC and acinar clusters. The color bar at the top indicates mCherry-positive (magenta) and mCherry-negative (green)
1151 cell types. Expression level is highlighted with a color gradient. mCherry-positive cells showed higher expression of
1152 *dab2* and other LRE enriched endocytic markers (bolded), whereas mCherry-negative cells express typical anterior
1153 enterocyte markers such as *fabp2*.
1154

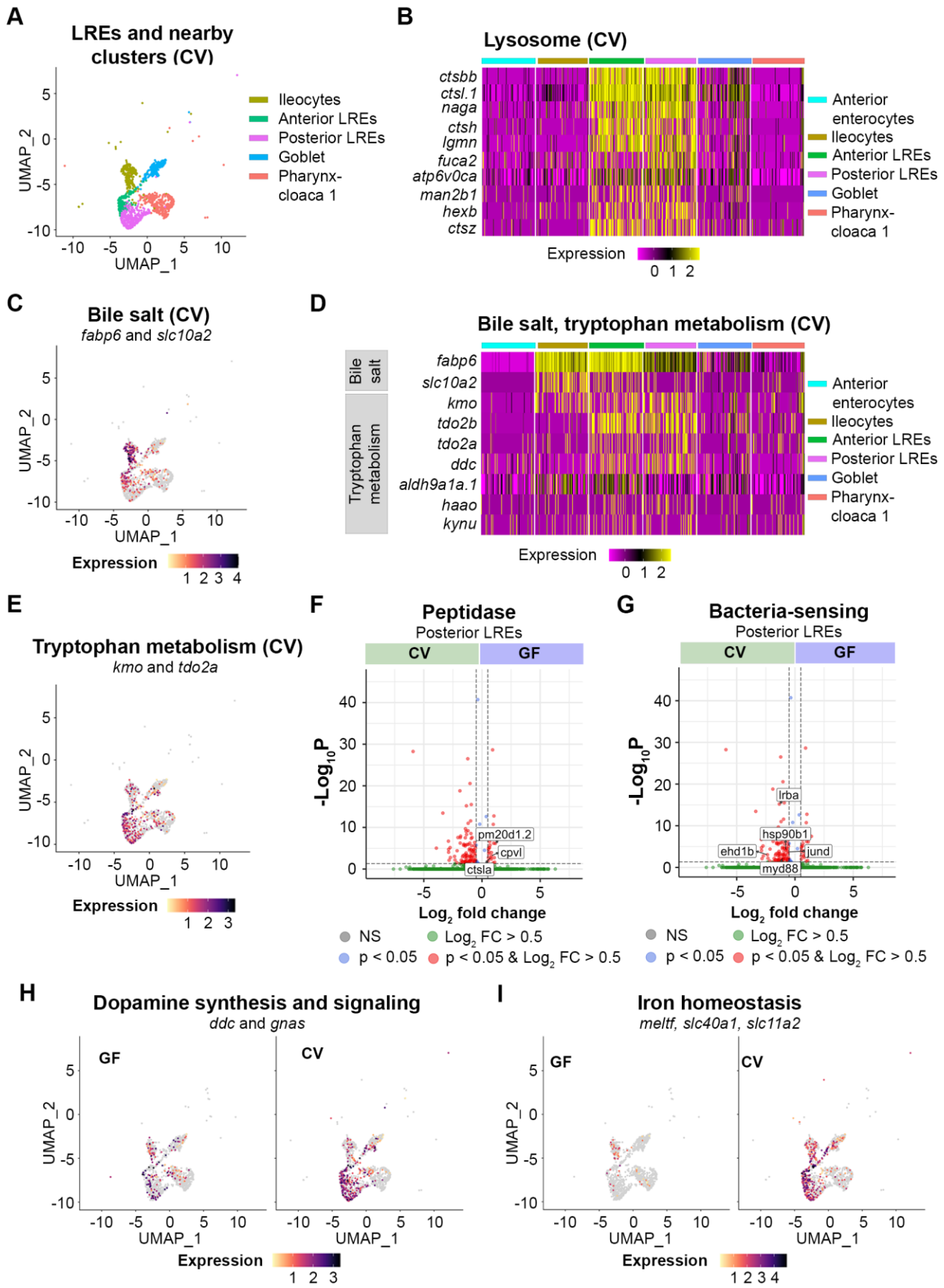
A
LREs and nearby clusters (CV)
Ileocytes
Anterior LREs
Posterior LREs
Goblet
Pharynx-cloaca 1
UMAP_2
UMAP_1
B
Lysosome (CV)
ctsbb
ctsl.1
naga
ctsh
lgmn
fuca2
atp6v0ca
man2b1
hexb
ctsz
Anterior enterocytes
Ileocytes
Anterior LREs
Posterior LREs
Goblet
Pharynx-cloaca 1
Expression
0 1 2
C
Bile salt (CV)
fabp6 and slc10a2
Expression
1 2 3 4
D
Bile salt, tryptophan metabolism (CV)
Bile salt
Tryptophan metabolism
fabp6
slc10a2
kmo
tdo2b
tdo2a
ddc
aldh9a1a.1
haao
kynu
Expression
0 1 2
E
Tryptophan metabolism (CV)
kmo and tdo2a
Expression
1 2 3
F
Peptidase
Posterior LREs
CV
GF
-Log10P
Log2 fold change
pm20d1.2
cpvl
ctsla
NS
Log2 FC > 0.5
p < 0.05
p < 0.05 & Log2 FC > 0.5
G
Bacteria-sensing
Posterior LREs
CV
GF
-Log10P
Log2 fold change
lrba
hsp90b1
ehd1b
jund
myd88
NS
Log2 FC > 0.5
p < 0.05
p < 0.05 & Log2 FC > 0.5
H
Dopamine synthesis and signaling
ddc and gnas
GF
CV
UMAP_2
UMAP_1
Expression
1 2 3
I
Iron homeostasis
meltf, slc40a1, slc11a2
GF
CV
UMAP_2
UMAP_1
Expression
1 2 3 4

1155

1156 **Figure 5. Transcriptomic patterns of anterior and posterior LREs.**
1157 (A) UMAP projection shows anterior and posterior LREs, as well as close cell clusters in the CV condition. Cell types
1158 are color coded.
1159 (B) Heatmap illustrates expression of lysosome KEGG pathway genes in LREs and close clusters. The colored bars at
1160 the top of the plot indicate the cluster. Heatmap color corresponds to expression intensity.
1161 (C) UMAP projection displays expression of the bile salt transport genes *fabp6* and *slc10a2* in the LREs, ileocytes,
1162 goblet and pharynx-cloaca 1 cells. Cell color indicates cumulative expression intensity for *fabp6* and *slc10a2*.
1163 (D) Heatmap highlights expression of bile salt transport and tryptophan metabolism genes in the LREs and close
1164 clusters. The colored bars at the top indicate the cell cluster.
1165 (E) UMAP projection displays expression of tryptophan metabolism genes *kmo* and *tdo2a* in the LREs and close
1166 clusters. Cell color indicates cumulative expression intensity of *kmo* and *tdo2a*.
1167 (F) Volcano plot shows DEGs between GF and CV posterior LREs. Peptidase genes are tagged.
1168 (G) Volcano plot shows DEGs between GF and CV posterior LREs. Genes involved in microbe sensing and
1169 inflammatory response are tagged.
1170 (H) UMAP projection plots show expression of dopamine synthesis (*ddc*) and signaling (*gnas*) genes in GF (left) and
1171 CV (right) cells.
1172 (I) UMAP projection plots show expression of iron homeostasis genes (*meltf*, *slc40a1*, *slc11a2*) in GF (left) and CV
1173 (right) cells.

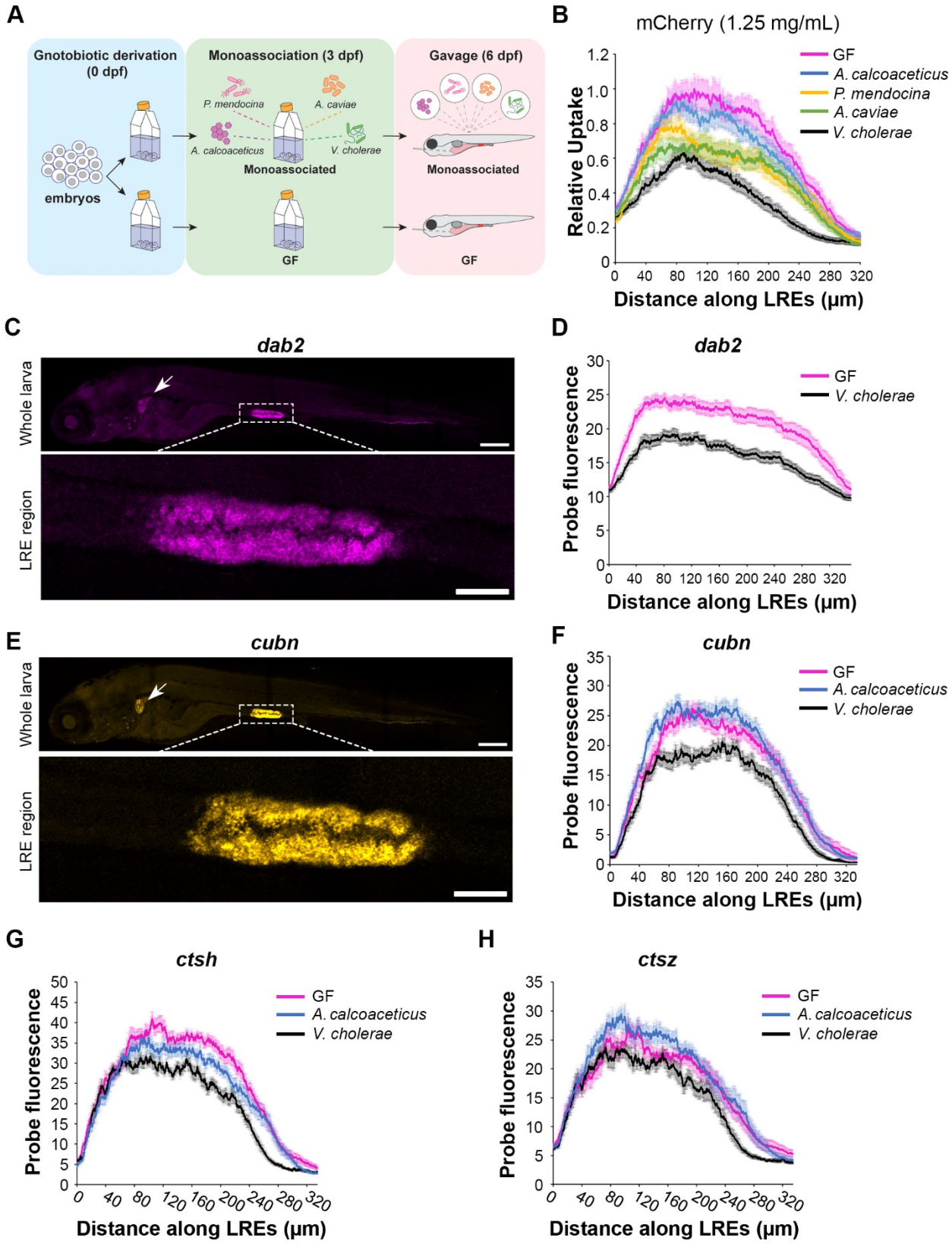
A
Gnotobiotic derivation (0 dpf)
Monoassociation (3 dpf)
Gavage (6 dpf)
P. mendocina
A. caviae
A. calcoaceticus
V. cholerae
Monoassociated
Monoassociated
embryos
GF
GF
B
mCherry (1.25 mg/mL)
GF
A. calcoaceticus
P. mendocina
A. caviae
V. cholerae
Relative Uptake
Distance along LREs (µm)
C
dab2
Whole larva
LRE region
D
dab2
GF
V. cholerae
Probe fluorescence
Distance along LREs (µm)
E
cubn
Whole larva
LRE region
F
cubn
GF
A. calcoaceticus
V. cholerae
Probe fluorescence
Distance along LREs (µm)
G
ctsh
GF
A. calcoaceticus
V. cholerae
Probe fluorescence
Distance along LREs (µm)
H
ctsz
GF
A. calcoaceticus
V. cholerae
Probe fluorescence
Distance along LREs (µm)

1174
1175

1176 **Figure 6. LRE activity and expression of endocytic machinery are differentially affected by**
1177 **individual microbial strains.**
1178 (A) Cartoon of monoassociation experimental design. Following gnotobiotic derivation, monoassociated larvae are
1179 colonized with a single strain of bacteria at 3 dpf and gavaged with mCherry to measure protein uptake at 6 dpf.
1180 (B) Plot shows relative uptake of mCherry in larvae that were GF or monoassociated with a single bacterial strain.
1181 mCherry uptake was reduced by *A. calcoaceticus* (2-way ANOVA, $p = 0.0268$, $n = 19 - 20$), *P. mendocina* (2-way
1182 ANOVA, $p = 0.0033$, $n = 20 – 21$), *A. caviae* (2-way ANOVA, $p < 0.0001$, $n = 19 – 20$) and *V. cholerae* (2-way ANOVA,
1183 $p < 0.0001$, $n = 18 – 20$).
1184 (C) Confocal images show *dab2* HCR probe localization in whole zebrafish larva (top) and LRE region (bottom). Arrow
1185 points to pronephros. Whole larva scale = 200 μm. LRE region scale = 50 μm.
1186 (D) Plot shows *dab2* HCR probe fluorescence in the LRE region at 6 dpf. *dab2* expression was significantly greater in
1187 GF than *V. cholerae*-colonized larvae (2-way ANOVA, $p < 0.0001$, $n = 23$).
1188 (E) Confocal images show *cubn* HCR probe localization in whole zebrafish larva (top) and LRE region (bottom). Arrow
1189 points to pronephros. Whole larva scale = 200 μm. LRE region scale = 50 μm.
1190 (F) Plot shows *cubn* HCR probe fluorescence in the LRE region at 6 dpf. There was greater *cubn* expression in *A.*
1191 *calcoaceticus*-colonized than GF larvae (2-way ANOVA, $p = 0.049$, $n = 21 – 23$), but *V. cholerae* significantly reduced
1192 *cubn* expression (2-way ANOVA, $p < 0.0001$, $n = 16 – 23$).
1193 (G) Plot of *ctsh* expression in GF and monoassociated larvae. GF larvae showed greater *ctsh* expression than *A.*
1194 *calcoaceticus* (2-way ANOVA, $p = 0.0183$, $n = 10 - 12$) or *V. cholerae*-colonized larvae (2-way ANOVA, $p < 0.0001$, n
1195 = 8 - 12).
1196 (H) Plot of *ctsz* expression in GF and monoassociated larvae. *A. calcoaceticus* and GF larvae showed similar levels of
1197 *ctsz* expression in LREs (2-way ANOVA, $p = 0.09$, n= 10 - 12). *V. cholerae* colonization reduced *ctsz* expression
1198 compared to GF larvae (2-way ANOVA, $p = 0.0014$, $n = 8 - 12$).

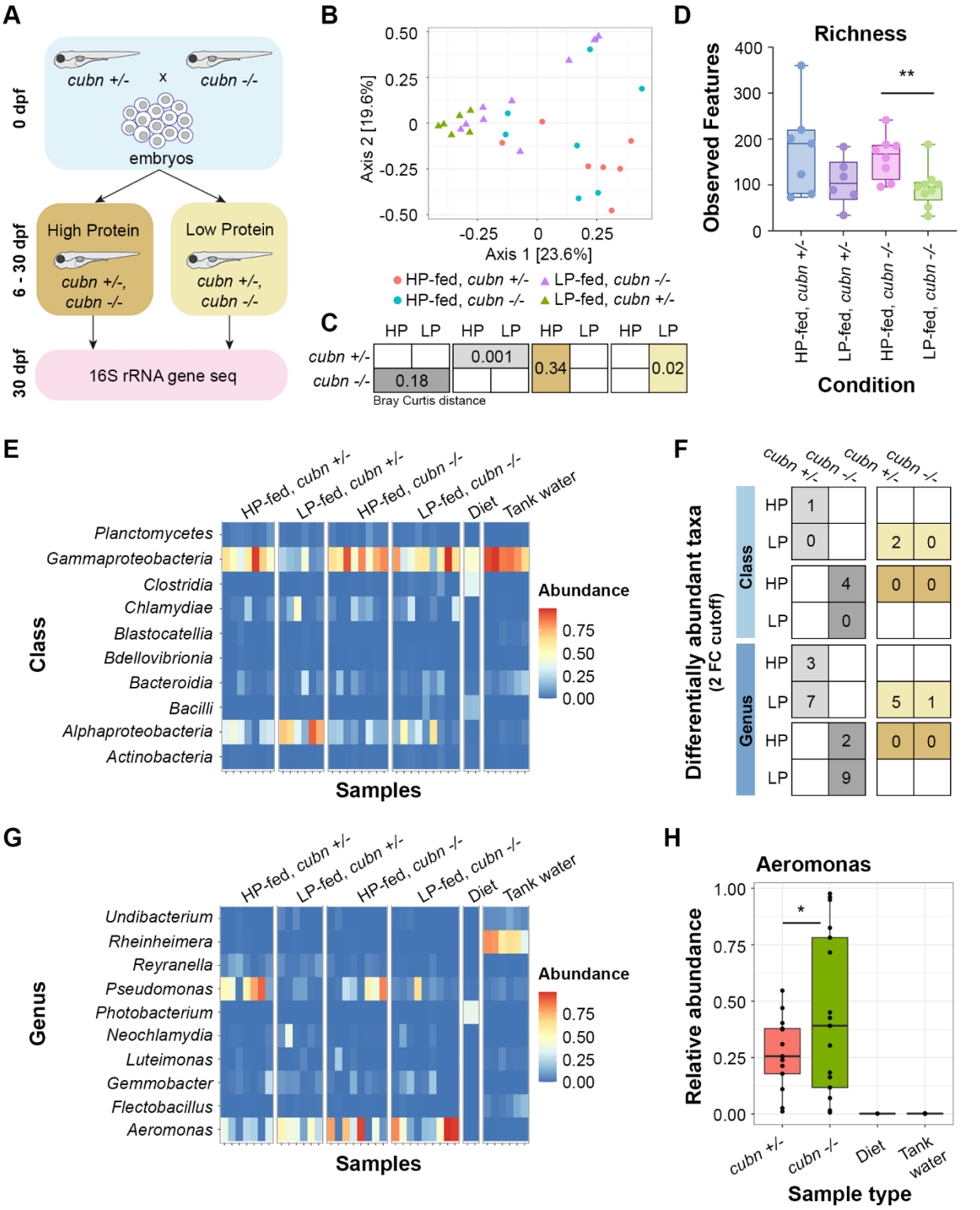

Figure 7. LRE activity and dietary protein impact gut microbiome.
(A) Cartoon of 16S rRNA gene sequencing experimental design. Homozygous *cubn* mutant and heterozygote larvae from the same clutch were fed a HP or LP diet from 6 to 30 dpf prior to whole larvae DNA extraction.
(B) MDS plot of Bray Curtis distance between zebrafish samples.
(C) Boxes show Bray Curtis distance p-values comparing genotype and diet effects on beta diversity.
(D) Box plot of observed features between conditions.

1206 (E) Heat map of classes with the highest relative abundance across all samples.
1207 (F) Table of differentially abundant taxa counts at the class and genus levels. Boxes show the number of differentially
1208 abundant taxa per compared condition. Dietary comparisons are in the left column. Genotype comparisons are in the
1209 right column.
1210 (G) Heat map of the genera with the highest relative abundance across all samples.
1211 (H) Box plot showing relative abundance of *Aeromonas* spp. across genotypes and controls. The relative abundance
1212 of *Aeromonas* spp. was significantly higher in *cubn* mutants than heterozygotes (DESeq2, padj = 0.01).

1213

1214

1215

1216

1217

1218